Earth-Science Reviews 201 (2020) 102958

Contents lists available at ScienceDirect

Earth-Science Reviews

journal homepage: www.elsevier.com/locate/earscirev

Seafloor massive sulfides from mid-ocean ridges: Exploring the causes of their geochemical variability with multivariate analysis

Luca Toffolo[a], Paolo Nimis[a,*], Gennady A. Tret'yakov[b], Irina Y. Melekestseva[b], Victor E. Beltenev[c]

[a] Dipartimento di Geoscienze, Università degli Studi di Padova, Via Gradenigo 6, Padova 35131, Italy
[b] South Urals Federal Research Center, Urals Branch of Russian Academy of Sciences, Institute of Mineralogy, Chelyabinsk District, Miass 456317, Russia
[c] Polar Marine Geosurvey Expedition, Pobedy st. 24, Lomonosov–St. Petersburg 198412, Russia

ARTICLE INFO

Keywords:
Seafloor massive sulfides
Mid-ocean ridges
Geochemistry
Multivariate analysis

ABSTRACT

The neovolcanic zones of mid-ocean ridges are host to seawater-derived hydrothermal systems forming seafloor massive sulfide (SMS) deposits. These deposits have high concentrations of base metals and potentially economic enrichment of a wide range of trace elements. The factors controlling this enrichment are currently poorly understood. We have investigated the main factors controlling SMS compositional variability through robust principal component analysis and robust factor analysis of published and newly obtained bulk geochemical data for samples collected from SMS deposits worldwide. We found that a large part of the observed variability is produced by a combination of three independent factors, which are interpreted to reflect (in order of importance): (1) the temperature of deposition, (2) the ridge spreading rate, and (3) zone refining. The first and the third factors are mostly related to processes operating near the seafloor, such as conductive cooling, mixing of the hydrothermal fluids with seawater and metal remobilization, and determine the relative proportions of the main minerals and, thus, of Cu and Zn (Co, Se, Sb, Pb). The ridge spreading rate influences the structure of the oceanic lithosphere, which exerts a major control on the length and depth of the hydrothermal convection cell and on the rock-to-water ratios in the reaction zone, which in turn control the behavior of the precious metals Au and Ag and elements including Ni (Mo, Se). Despite the obvious role of substrate rocks as metal sources, their composition (specifically mafic vs. ultramafic) does not emerge as a statistically significant independent factor.

1. Introduction

Seafloor massive sulfides (SMS) are stratiform or stratabound accumulations of base metal sulfides that formed on or near the seafloor by precipitation from dominantly seawater-derived hydrothermal fluids (Hannington, 2014). Since their discovery in 1978 at the East Pacific Rise (Francheteau et al., 1979), SMS deposits have been recognized along many neovolcanic plate boundaries, including mid-ocean ridges, submarine arc volcanoes and back-arc spreading centers. In all these environments, magma intrusions sustain hydrothermal convective cells, in which percolating seawater leaches metals from the substrate rocks (Sleep, 1983; Tivey, 2007). Upon ascent, metals precipitate primarily as sulfides below and on the seafloor, as the hot (up to ~400 °C) and acidic (pH at 25 °C as low as ~3) hydrothermal fluid quenches in the presence of cold (~2 °C) and alkaline (pH at 25 °C ~ 8) seawater. Considering the total length of neovolcanic plate boundaries, SMS deposits could represent a significant source of metals, estimated at ~3×10^7 t of Cu + Zn (Hannington et al., 2011). Moreover, some deposits have remarkable grades of gold and silver (up to several tens of ppm; Petersen and Hein, 2013). Unraveling the factors that affect the geochemistry of SMS is important to the understanding of their genesis and for developing effective guidelines for the exploration and economic evaluation of both present-day seafloor deposits and their ancient on-land analogues.

Observations on SMS deposits show that the geochemistry of the massive sulfides is primarily related to the geodynamic setting in which they are formed. On mid-ocean ridges, where the hydrothermal fluids dominantly leach mafic or ultramafic substrates, SMS typically have high concentrations of Cu + Zn (> > Pb) (Hannington et al., 2005). The leaching of elements from substrate rocks is influenced by the structure of the oceanic lithosphere and by the nature of the hydrothermal convection, which are essentially related to the spreading rate (Bougault et al., 1993; Bach and Humphris, 1999; Coumou et al., 2009). On *slow-spreading* ridges, for instance, the magma supply is low and part of the extension is accommodated by deep-rooted detachment faults. Therefore, the lithosphere is not layered and is mainly composed of

* Corresponding author.
E-mail address: paolo.nimis@unipd.it (P. Nimis).

https://doi.org/10.1016/j.earscirev.2019.102958
Received 2 February 2019; Received in revised form 6 September 2019; Accepted 11 September 2019
Available online 13 September 2019
0012-8252/

Table 1
Massive sulfides samples from Irinovskoe, Krasnov and Peterburskoe hydrothermal sites on the Mid-Atlantic Ridge.

Sample number	Sample description	Sampling mode	Coordinates		Mineral assemblage												
			Latitude	Longitude	Ccp	Py/Mrc	Sp/Wur	Sec. Cu-sulf.	Opl/Qtz	Anh	Brt	Cb	Fe-oxyhydr.	Mn-oxyhydr.	Tlc	"atc"	Jrs
Irinovskoe																	
34L 227-1a	Fragment of coalesced Mrc–Ccp smoker chimneys	Dredge	13° 20,089′ 13° 19,744″	44° 54,572′ 44° 54,786’	+++	++	−	+	+	−	tr	−	+	+	tr	+	−
34L 227-1b	As above	Dredge	13° 20,089′ 13° 19,744’	44° 54,572′ 44° 54,786’	+++	++	−	+	+	−	tr	−	+	+	tr	+	−
34L 227-2	As above	Dredge	13° 20,089′ 13° 19,744’	44° 54,572′ 44° 54,786’	+++	++	−	+	+	−	tr	−	+	+	tr	+	−
34L 227-3	Fragment of a single Mrc–Ccp smoker chimney	Dredge	13° 20,089′ 13° 19,744’	44° 54,572′ 44° 54,786’	+++	++	−	+	+	−	tr	−	+	+	tr	+	−
34L 227-4	Fragment of coalesced Mrc-Ccp smoker chimneys	Dredge	13° 20,089′ 13° 19,744’	44° 54,572′ 44° 54,786’	+++	++	−	+	+	−	tr	−	+	+	tr	+	−
34 L 240-1-3	Massive Ccp-Sp-Mrc	TV-grab	13° 19,953’	44° 54,653’	+	++	+	+	++	−	+	−	−	−	−	−	−
34L 241-1/1	Massive Sp–Py–Ccp from the basement of a large sulfide edifice	TV-grab	13° 19,957’	44° 54,679’	++	+	++	+	+	tr	−	−	−	−	−	−	−
34L 241-2/2	Massive Py–Ccp–Sp ore from the intermediate part of a large sulfide edifice	TV-grab	13° 19,957’	44° 54,679’	++	++	++	+	−	tr	−	−	−	−	−	−	−
34L 241-2/3	Massive Py–Ccp–Sp from the top of a large sulfide edifice	TV-grab	13° 19,957’	44° 54,679’	+	+	+++	+	+	tr	−	−	−	−	−	−	−
34L 245-1	Massive Py (with fine-grained and, locally, crystalline aggregates)	Dredge	13° 20,785′ 13° 20,898’	44° 54,948′ 44° 55,319’	−	+++	−	−	tr	−	+	−	−	−	−	−	−
34L 246-1/1	Massive Py–Ccp with numerous channels and concentrically-zoned structures	TV-grab	13° 19,925	13° 19,925	++	++	−	+	+	−	−	−	−	−	−	−	−
34L 246-1/9	As above	TV-grab	13° 19,925	13° 19,925	++	++	−	+	+	−	−	−	−	−	−	−	−
34L 247-1/1	Strongly oxidized massive Ccp with channels and concentrically-zoned structures	TV-grab	13° 19,996’	44° 54,641’	++	++	−	++	+	−	−	tr	+	+	−	−	−
34L 250 1/1	Banded Ccp-Py	Dredge	13° 20,627′ 13° 20,697’	44° 56,371′ 44° 55,744’	++	+++	−	++	−	−	−	tr	−	−	−	−	−
34L 250 2/2	Strongly oxidized sulfide breccia (clasts: Py + Ccp; matrix: Brt, Arg, Opl, sulf.)	Dredge	13° 20,627′ 13° 20,697’	44° 56,371′ 44° 55,744’	++	++	−	−	++	−	++	++	−	−	−	−	−
Krasnov																	
1271	Massive coarse-crystalline Py	TV-grab	16°38.424’	46°28.543’	−	+++	−	−	−	−	−	−	−	−	−	−	−
1269	Massive coarse-crystalline Py	TV-grab	16°38.448’	46°28.504’	−	+++	−	−	−	−	−	−	−	−	−	−	−
Peterburskoe																	
34L 93-2	Porous fine-grained Py-Fe-oxyhydr.	Dredge	19° 52,600′ 19° 52,659’	45° 52,606′ 45° 52,898’	−	+++	−	−	tr	−	tr	tr	++	tr	tr	tr	−
34L 95-1	Massive porous fine-grained Py–Cv–Ccp	Dredge	19° 52,873′ 19° 52,691’	45° 52,402′ 45° 52,615’	++	+	−	++	++	−	tr	tr	+	+	−	−	+
34L 95-2	Py breccia with massive, colloform, banded clasts; the amount of clasts is up to 80%	Dredge	19° 52,873′ 19° 52,691’	45° 52,402′ 45° 52,615’	tr	+++	−	−	tr	−	tr	−	−	−	tr	−	−
34L 95-3	Massive Py ore with numerous fractures and vugs	Dredge	19° 52,873′ 19° 52,691’	45° 52,402′ 45° 52,615’	+	+++	−	−	−	−	−	−	+	−	+	−	−
34L 95-4	Massive Ccp–Py	Dredge	19° 52,873′ 19° 52,691’	45° 52,402′ 45° 52,615’	+	+++	−	+	−	−	−	−	+	−	+	+	−
34L 176-4	Massive Cv–Py–Mrc	TV-grab	19° 53,115’	45° 52,352’	tr	+++	−	++	tr	tr	tr	−	tr	−	−	tr	−
34L 176-5	As above	TV-grab	19° 53,115’	45° 52,352’	tr	+++	−	++	tr	tr	tr	−	tr	−	−	tr	−
34L 176-8	As above	TV-grab	19° 53,115’	45° 52,352’	tr	+++	−	++	tr	tr	tr	−	tr	−	−	tr	−
34L 176-11	As above	TV-grab	19° 53,115’	45° 52,352’	tr	+++	−	++	tr	tr	tr	−	tr	−	−	tr	−

(*continued on next page*)

Table 1 (*continued*)

Sample number	Sample description	Sampling mode	Coordinates		Mineral assemblage											
			Latitude	Longitude	Ccp	Py/Mrc	Sp/Wur	Sec. Cu-sulf.	Opl/Qtz	Anh	Brt	Cb	Fe-oxyhydr.	Mn-oxyhydr.	Tlc	"atc"	Jrs
34L 174-1	Colloform, porous, dendritic, locally, massive Py–Mrc	TV-grab	19° 52,550'	45° 52,693'	–	+ + +	–	+	–	tr	+	tr	+	–	–	+	–
34L 174-3	As above	TV-grab	19° 52,550'	45° 52,693'	–	+ + +	–	+	–	tr	+	tr	+	–	–	+	–
34L 174-4	As above	TV-grab	19° 52,550'	45° 52,693'	–	+ + +	–	+	–	tr	+	tr	+	–	–	+	–
34L 174-5	As above	TV-grab	19° 52,550'	45° 52,693'	–	+ + +	–	+	–	tr	+	tr	+	–	–	+	–

Modal abundances: (+ + +): > 50 vol%; (+ +): 50–11 vol%; (+): 10–2 vol%; (tr.): ≤ 1 vol%. Mineral abbreviations: Anh: anhydrite; "atc": atacamite group minerals; Brt: barite; Cb: carbonates; Ccp: chalcopyrite; Fe-oxyhydr.: Fe-oxyhydroxides; Mn-oxyhydr.: Mn-oxyhydroxides; Mrc: marcasite; Jrs: jarosite; Opl/Qtz: opal/quaryz; Py: pyrite; Sp/Wur: sphalerite/wurtzite; Sec. Cu sulf.: secondary Cu sulfides; Tlc: talc.

gabbros and ultramafic rocks (MacLeod et al., 2009; Lowell, 2010). In this setting, low heat fluxes and deep-rooted faults favor long and deep fluid pathways, which enhance fluid-rock interaction at relatively high rock-to-water (r/w) ratios (Bach and Humphris, 1999). By contrast, on *fast-spreading* ridges, the magma supply is high, the lithosphere is typically layered and the upper basaltic section is highly permeable (Coumou et al., 2008). The resulting higher heat flux, together with episodic diking events, favor the development of shallower and ephemeral hydrothermal convection cells (Wilcock and Delaney, 1996). Therefore, fast-spreading ridges are typified by less evolved seawater-dominated fluids (i.e., lower r/w ratios). Irrespective of spreading rate, SMS deposits show significant geochemical variability along the same ridge and even at the deposit or hand-specimen scale (Petersen and Hein, 2013), suggesting a complex interplay of regional and local controls. In fact, some specific geochemical features (e.g., Au enrichment and Au/Ag and Co/Ni ratios) have been variably related to the nature of the substrate (e.g., mafic vs. ultramafic rocks), phase separation processes in the fluid, the presence of a magmatic influx of volatiles and metals, the morphology of vent structures (tubular vs. beehive chimneys generated by focused or diffuse fluid flow, respectively), the ridge spreading rate, or a combination of these factors (Marques et al., 2006; Fouquet et al., 2010; German et al., 2016; Melekestseva et al., 2017; Knight et al., 2018). However, the relative role of these factors in controlling the geochemical variability of SMS deposits is still poorly defined. Part of this uncertainty is due the fact that the nature of the substrate is inferred from two-dimensional seafloor observations and different lithologies may occur in the areas surrounding the deposits. Also, individual deposits may show a mixture of apparent geochemical signatures (e.g., 'mafic' and 'ultramafic'; Marques et al., 2006; Webber et al., 2015; Melekestseva et al., 2017). Moreover, experimental works on rock/seawater interactions under conditions typical of subseafloor reaction zones so far mainly explored the behavior of only a few base metals (Fe, Mn, Zn, Cu, Ni) in basalt-seawater systems at r/w ratios ranging from ~0.001 to 2 (Seyfried and Bischoff, 1977; Seyfried Jr. and Bischoff, 1981; Seyfried Jr. and Mottl, 1982; Seyfried Jr. and Janecky, 1985; Seewald, 1990). Experiments on peridotite-seawater systems investigated even fewer base metals (Fe, Mn, Ni, Zn) and only at r/w < 0.1 and $T \leq 300$ °C (Seyfried, 1980; Janecky, 1986). Forward thermodynamic modeling of rock-seawater reactions and hydrothermal fluid cooling has been used to investigate the behavior of a larger number of elements in seafloor hydrothermal systems (Janecky, 1984; McCollom and Shock, 1998; Wetzel and Shock, 2000; Palandri and Reed, 2004; Klein et al., 2013; Melekestseva et al., 2014, 2017; Fuchs et al., 2019). However, the resulting models are specific to particular rock compositions reacting under fixed conditions or to particular fluid compositions and are not generally applicable to all hydrothermal systems on mid-ocean ridges.

In this work, we investigate the first-order controls on the compositions of SMS deposits on mid-ocean ridges by means of multivariate statistical analysis of published and novel bulk chemical analyses of SMS samples from seafloor hydrothermal fields worldwide. Attempts to apply multivariate statistical analysis to SMS at various scales were previously made by Hannington et al. (1991a) and Fouquet et al. (2010). Hannington et al. (1991a) applied factor analysis to mafic-hosted deposits worldwide and found important geochemical associations for Sb-Pb-Au-Ag and Mo-Co-Se-Cu-Fe, reflecting metal associations of low- and high-temperature mineral assemblages, respectively. Fouquet et al. (2010) used principal component analysis to identify site-specific geochemical groups (i.e., Cu-rich high-temperature, Zn-rich intermediate-temperature, and oxide/sulfate, respectively) in ultramafic-hosted deposits at the Mid-Atlantic Ridge. Compared with these previous works, the dataset considered here is more comprehensive as it is built on four times the sample number analyzed by Hannington et al. (1991a), covers more ridges and includes data from both mafic- and ultramafic-hosted SMS deposits. Moreover, in this work we use robust principal component analysis (rPCA) and robust factor analysis

(rFA) to limit the influence of noise from individual anomalous samples. This is particularly useful, because analyzed SMS materials mostly consist of dredged samples and are certainly affected by sampling bias (Fuchs et al., 2019). Therefore, our analysis provides a better assessment of the first-order factors that control the geochemical variability of ridge-hosted SMS at a global scale. By comparing the results with existing experimental data and new thermodynamic models, we show that temperature of deposition, seafloor spreading rate and r/w ratio, and zone refining are the major factors controlling metal associations in SMS deposits and that, contrary to common belief, the nature of the substrate may be of secondary importance.

2. Materials and methods

Based on an initial database by Hannington et al. (2004), we have compiled published and unpublished bulk chemical analyses of sulfides samples collected from SMS deposits located on mid-ocean ridges. New analyses of samples from the Irinovskoe, Krasnov and Peterburgskoe SMS fields at the Mid-Atlantic Ridge (Table 1) were acquired at the South Urals Federal Research Center, Urals Branch of Russian Academy of Sciences, Institute of Mineralogy (Miass, Russia) using atomic absorption (AA) analysis in air-acetylene flame on a Perkin Elmer 3110 spectrometer (Co, Ni, Cu, Zn, Pb, Au, Ag) and inductively coupled plasma-mass spectrometry (ICP MS) on an Agilent 7700× mass spectrometer (Sb, Se, Mo). For AA analyses of Co, Ni, Cu, Zn and Pb, 0.5–1.0 g of sample material was dissolved in a 15-ml mixture of HF, HCl, and HNO_3, heated first up to 100–150 °C and then to 250 °C, and concentrated to the formation of wet salts. This procedure was conducted three times, then the samples were dried, cooled, mixed with 3 ml concentrated HNO_3, and filtered. For AA analyses of Au and Ag, 1 g of sample material was diluted in a mixture of 30 ml HCl and 10 ml HNO_3, concentrated on the oven to the formation of wet salts, filtered using HCl solution and cooled. For ICP-MS analyses, the sample material was initially digested in Teflon autoclaves using a mixture of HF, HCl and HNO_3 in a SpeedWave microwave digestion system (Berghof, Germany) using a two-stage heating procedure to a temperature of up to 180 °C for 40 min. After digestion, the fluorine complexes were decomposed by double evaporation of the dry residual with concentrated HNO_3 at 110 °C in glassy carbon crucibles. The precipitates were further dissolved in hot 0.5 N HNO_3 and subsequently reduced to a 100-ml aliquot. All pure acids used for digestion were purified in a BSB-939-IR apparatus (Berghof, Germany). The water for dilution was deionized in a Milli-Q® Integral Water Purification System by Millipore, US. Quality control of the analytical procedure was performed by analysis of state reference materials (GSO) of water metal solutions (7256-96 Zn, 7252-96 Pb, 7265-96 Ni, 7268-96 Co, 7255-96 Cu, and 8402-2002 Ag) and flotation concentrate of Au-bearing ore CZK-3 (2739-83 Au) for AA analysis. Indium was used as an internal standard calibrated against the USGS BCR-2 rock reference material for ICP MS analyses.

For the statistical analysis, we only considered reportedly fresh SMS samples representing fragments of hydrothermal chimneys and mounds. We excluded samples which contained significant proportions of weathering products or silicate gangue (e.g., Al_2O_3 content > 2 wt %). The presence of silica phases, which do not typically contain significant trace elements, was not considered critical. Since the chemical analyses were heterogeneous in terms of analyzed elements and their detections limits, we only selected those records that provided data for a sufficiently large number of elements (i.e., Au, Ag, Co, Mo, Ni, Sb, Se, Cu, Zn, Pb). Barite-rich (Ba > 1 wt%) samples were excluded to avoid possible bias caused by elements (Pb, Co, Ni, Sb) incorporated in or adsorbed on barite (cf. Melekestseva et al., 2014; Safina et al., 2016). Analyses reported only as averages of several samples were discarded, since these data were not accompanied by adequate mineralogical and textural descriptions of individual samples. These choices allowed us to maintain a balance between the number of elements (N = 10), the number of records (N = 426) and the number of represented hydrothermal sites or clusters (N = 26; Table 2). For instance, due to the incompleteness of many published analyses, adding a single element such as As would have decreased the number of represented sites to 25 (the Beebe hydrothermal field would be completely excluded). The SMS deposits were grouped on the basis of the ridge spreading rate [fast, intermediate, and (ultra)slow] and host-rock composition (mafic or ultramafic). The complete database (Table S1) includes samples from 3 sites on fast, 8 sites on intermediate, 12 sites on slow, and 3 sites on ultraslow spreading ridges (Table 2). The distinction between mafic-hosted and ultramafic-hosted deposits was not always straightforward, because both types of rocks generally occur in the areas surrounding and probably beneath nominally ultramafic-hosted deposits. In this work, deposits classified as ultramafic-hosted ($N_{ultramafic}$ = 6 out of a total of 26) are those sited on substrates that, based on reported geological evidence, are likely to contain abundant ultramafic rocks (Table 2). The resulting mafic-hosted vs. ultramafic-hosted classification is the same as that used in the recent review by Fuchs et al. (2019).

The statistical relationships between elements were explored by using both non-parametric and parametric techniques for dimension reduction, i.e., rPCA and rFA, respectively. The former technique has the advantage of not being influenced by the user's decisions and is, therefore, more appropriate at an exploratory stage. The latter technique is dependent on the number of chosen factors, but, unlike rPCA, it does not force the factors to explain all the variability (Reimann et al., 2008). Therefore, rFA may be more effective in defining statistical factors that are representative of common geochemical processes (Reimann et al., 2002). Accordingly, we used rPCA to guide rFA, in the sense that the number of principal components that explained most of the variability in rPCA were used to determine the proper number of factors for rFA (Reimann et al., 2008). The statistical analyses were performed with the R software using the function “pcaCoDa” in the “robCompositions” library (Templ et al., 2011) and the R script (principal factor analysis with a varimax rotation) by Filzmoser et al. (2009a). Robust methods were preferred to “classical” methods, because they are less sensitive to outliers (Filzmoser et al., 2009b; Filzmoser and Hron, 2011), which are common in geochemical data. Isometric logratio and centered logratio transformations were applied to the data used for rPCA and rFA, respectively. These transformations have the advantage of opening the data, but require that no zeros are present in the data matrix. Therefore, we represented concentrations below the detection limit by multiplying the detection limit by 0.65. This choice is statistically appropriate since only 5.3% of the data are below detection limit (Palarea-Albaladejo and Martín-Fernández, 2015; Martín-Fernández et al., 2003).

To obtain independent constraints for the interpretation of the statistical data, we simulated the basalt–seawater and peridotite–seawater reactions in a model subseafloor hydrothermal reaction zone. Thermodynamic calculations were performed by Gibbs energy minimization using the Selektor program (Karpov et al., 1997; Chudnenko, 2010). Rock–seawater reactions were modeled at 400 °C and 30 MPa assuming various r/w ratios. Complete details on the modeling procedure and the choice of thermodynamic data are reported in Melekestseva et al. (2017). The compositions of basaltic glass and peridotite were taken from Lehnert et al. (2000) and Fouquet et al. (2010), respectively. Molybdenum content in basalt (0.31 ppm) and seawater (1.04×10^{-7} mol/kg H_2O) were taken from Fouquet et al. (2010) and Steele et al. (2010), respectively. Seawater and reactant rock compositions are reported in Table S2.

3. Results

3.1. Element distribution

The distribution of elements in mid-ocean ridge SMS is reported in Table 2 and illustrated by box-and-whiskers plots in Fig. 1. Median element concentrations include ~2 wt% Cu, ~0.7 wt% Zn, ~0.01 wt% Pb, ~300 ppb Au, ~100 ppm Co, ~60 ppm Se, ~50 ppm Mo, ~20 ppm Ag, ~10 ppm Ni, and ~5 ppm Sb.

Table 2
Elements distribuiton in massive sulfides from mid-ocean ridges. Ultramafic-hosted sites are underlined.

Sites	Spreading rate at site	Host rock	Depth (m)	n	Au (ppb)			Ag (ppm)			Co (ppm)		
					1st quartile	Median	3rd quartile	1st quartile	Median	3rd quartile	1st quartile	Median	3rd quartile
Explorer Ridge													
Southern Explorer Ridge	Intermediate (~56 mm/a)	MORB	1800–1850	17	170.00	180.00	380.00	9.50	24.00	51.00	390.00	920.00	1400.00
Juan de Fuca													
Main Field	Intermediate (~56 mm/a)	MORB	2000–2220	28	12.25	40.50	61.00	3.78	11.05	44.40	4.25	40.00	167.50
Mothra Field	Intermediate (~56 mm/a)	MORB	2270	3	1.30	1.30	16.00	2.10	33.30	38.30	2.00	88.00	130.00
Axial seamount	Intermediate (~56 mm/a)	MORB	1540	5	123.50	1950.00	3820.00	14.25	82.90	247.25	0.65	2.00	8.50
Middle Valley, Bent Hill	Intermediate (< 54 mm/a)	MORB, sediments	2400	35	14.00	44.00	108.00	2.00	3.00	4.30	5.70	9.20	54.00
Gorda Ridge													
Escanaba Trough	Intermediate (~55 mm/a)	MORB, sediments	3210–3280	10	130.00	1120.00	1920.00	3.50	9.50	62.25	195.00	485.00	917.50
East Pacific Rise													
21° N	Intermediate (~63 mm/a)	MORB	2000	14	32.50	76.00	130.00	7.95	19.00	39.75	15.00	40.00	173.75
13° N	Fast (~91 mm/a)	MORB	2600–2630	11	72.00	412.00	1024.00	4.00	68.00	136.00	59.00	148.00	377.00
7° 24′ S	Fast (~137 mm/a)	MORB	2700–2750	13	11.00	63.00	72.00	11.50	20.00	35.00	427.50	758.00	1200.00
16° 43′ S	Fast (~146 mm/a)	MORB	2600	19	72.00	240.00	480.00	26.00	44.00	70.00	205.00	799.00	1100.00
Galapagos Rift													
	Intermediate (63–66 mm/a)	probably MORB	2600	62	57.00	215.00	310.00	12.75	21.50	33.93	40.75	153.50	382.50
Mid-Cayman Rise													
Beebe	Ultraslow (~17 mm/a)	MORB, probably ultramafics	4960	26	3065.00	6615.00	19,900.00	14.48	52.40	128.25	55.70	150.50	325.75
Mohns Ridge													
Loki's Castle	Ultraslow (~15 mm/a)	MORB	2400	4	115.50	218.50	288.50	2.93	3.75	9.83	3.30	28.75	85.63
Mid-Atlantic Ridge													
Semenov	Slow (~26 mm/a)	Ultramafics, MORB	2440	4	672.50	1725.00	41,687.50	10.58	43.50	206.18	15.50	32.50	122.55
Broken Spur	Slow (~23 mm/a)	MORB	3100	14	85.00	561.50	3867.50	2.95	16.85	68.43	6.50	66.50	220.00
Rainbow	Slow (~21 mm/a)	Ultramafics, gabbro, MORB	2270–2320	2	–	6035.00	–	–	25.60	–	–	5535.00	–
Logatchev 1	Slow (~26 mm/a)	Ultramafics, gabbro, MORB	2925–3050	12	625.00	3450.00	12,900.00	6.50	12.50	37.00	170.50	219.50	433.50

(*continued on next page*)

Table 2 (*continued*)

Sites	Spreading rate at site	Host rock	Depth (m)	n	Au (ppb)			Ag (ppm)			Co (ppm)		
					1st quartile	Median	3rd quartile	1st quartile	Median	3rd quartile	1st quartile	Median	3rd quartile
Peterburgskoe	Slow (~25 mm/a)	MORB	3400	14	205.00	430.00	1055.00	8.60	13.50	18.20	170.95	324.60	713.18
Irinovskoe	Slow (nd)	Ultramafics, gabbro	2700–2890	15	1040.00	2210.00	7530.00	24.50	37.60	57.60	106.50	167.00	263.30
TAG	Slow (~24 mm/a)	MORB	3435–3670	53	360	2400	8000	11	100	240	1.3	9	30.5
Snakepit	Slow (~24 mm/a)	MORB	3450–3500	22	162.50	414.50	1707.50	8.00	12.50	58.00	7.75	76.00	127.50
Krasnov	Slow (~25 mm/a)	MORB	3700–3900	2	–	1075.00	–	–	6.90	–	–	394.50	–
Southwest Indian Ridge													
Yuhuang-1	Ultraslow (nd)	Ultramafics, MORB	1400–1600	14	202.50	780.00	2715.00	17.15	37.90	95.73	20.78	36.10	88.58
Central Indian Ridge													
MESO Zone	Slow (~47 mm/a)	MORB	2850	6	235.00	740.00	1550.00	21.50	29.00	39.50	312.50	450.00	640.00
Kairei	Slow (~49 mm/a)	Ultramafics, MORB	2415–2460	17	321.00	1623.00	10,550.00	12.00	18.10	133.65	58.00	165.00	759.50
Edmond	Slow (~48 mm/a)	MORB	3290–3320	4	470.00	900.00	14,327.50	15.58	563.50	1365.00	128.75	648.00	1307.50
GLOBAL				426	72.00	288.50	1709.00	7.00	20.50	55.55	13.00	106.25	370.00

Sites	Mo (ppm)			Ni (ppm)			Sb (ppm)			Se (ppm)		
	1st quartile	Median	3rd quartile	1st quartile	Median	3rd quartile	1st quartile	Median	3rd quartile	1st quartile	Median	3rd quartile
Explorer Ridge												
Southern Explorer Ridge	150.00	250.00	350.00	0.50	7.00	9.75	3.50	4.50	30.00	61.50	130.00	175.00
Juan de Fuca												
Main Field	27.25	76.00	197.50	3.00	15.00	30.50	1.55	3.65	38.75	17.75	63.00	137.50
Mothra Field	0.65	0.65	2.00	2.00	10.00	10.00	0.07	0.60	1.20	8.00	300.00	420.00
Axial seamount	12.00	20.00	46.50	2.00	2.00	3.00	11.55	87.00	165.00	36.00	42.00	110.50
Middle Valley, Bent Hill	10.00	13.60	30.00	12.00	24.00	33.00	0.50	1.60	6.80	17.00	30.00	58.00
Gorda Ridge												
Escanaba Trough	12.25	22.00	48.00	1.63	9.00	19.75	4.00	16.50	163.00	78.75	134.50	167.75
East Pacific Rise												
21° N	8.75	24.50	57.75	2.94	3.25	37.00	1.00	2.50	11.50	9.75	109.00	223.25
13° N	19.00	34.00	98.00	3.25	27.00	62.00	2.00	6.00	22.00	1.20	17.00	182.00
7° 24′ S	65.50	103.00	152.50	28.00	28.00	33.00	1.90	4.00	6.00	39.00	60.00	195.00
16° 43′ S	61.00	134.00	255.00	25.00	28.00	33.00	1.70	6.80	13.00	50.00	110.00	220.00
Galapagos Rift												

(*continued on next page*)

Table 2 (*continued*)

Sites	Mo (ppm)			Ni (ppm)			Sb (ppm)			Se (ppm)		
	1st quartile	Median	3rd quartile	1st quartile	Median	3rd quartile	1st quartile	Median	3rd quartile	1st quartile	Median	3rd quartile
	104.25	121.00	194.00	8.00	33.00	46.00	4.00	6.45	10.60	32.75	81.00	145.50
Mid-Cayman Rise												
Beebe	21.18	39.90	74.88	0.84	1.77	6.72	1.19	3.61	27.43	5.35	20.50	71.55
Mohns Ridge												
Loki's Castle	1.98	19.50	39.50	0.74	2.00	3.75	1.25	2.10	5.20	338.75	415.00	461.25
Mid-Atlantic Ridge												
Semenov	17.75	50.30	87.65	12.25	25.00	29.50	1.94	8.63	59.00	1.55	11.85	215.20
Broken Spur	18.75	40.00	82.75	2.00	5.00	7.00	0.63	6.05	32.50	64.75	220.00	350.00
Rainbow	–	14.00	–	–	0.65	–	–	8.88	–	–	21.98	–
Logatchev 1	1.95	8.50	15.00	6.50	100.50	197.50	6.50	6.50	6.50	213.75	600.00	915.00
Peterburgskoe	31.70	50.42	86.01	3.92	5.35	9.23	1.10	2.31	2.98	44.75	62.69	83.68
Irinovskoe	11.06	26.02	32.81	4.60	6.89	14.32	2.35	4.08	5.67	19.22	184.65	374.44
TAG	43	68	127.5	6.5	13	21	4	21.7	112.25	3.25	3.25	9
Snakepit	12.75	20.50	37.25	6.50	18.00	44.00	1.88	5.15	14.58	26.25	117.50	221.75
Krasnov	–	47.65	–	–	5.12	–	–	1.69	–	–	4.94	–
Southwest Indian Ridge												
Yuhuang-1	6.85	12.30	16.88	4.00	6.35	9.28	1.23	2.00	3.70	0.83	1.95	4.45
Central Indian Ridge												
MESO Zone	134.75	290.00	352.50	19.50	24.50	30.75	1.08	2.35	5.25	50.25	300.00	430.00
Kairei	5.00	14.00	22.00	2.00	3.00	16.00	0.07	1.70	17.05	16.50	104.00	253.50
Edmond	19.05	119.10	243.75	5.00	9.00	29.50	2.45	54.10	107.25	10.00	15.00	20.00
GLOBAL	18.00	48.50	116.25	4.96	11.00	30.00	1.90	5.00	13.00	10.00	55.00	160.00

Sites	Cu (wt%)			Zn (wt%)			Pb (wt%)			Ref.
	1st quartile	Median	3rd quartile	1st quartile	Median	3rd quartile	1st quartile	Median	3rd quartile	
Explorer Ridge										
Southern Explorer Ridge	1.26	2.50	4.18	0.10	0.26	2.16	0.0150	0.0300	0.0400	1, 2
Juan de Fuca										
Main Field	0.16	1.50	4.28	0.08	0.46	19.60	0.0052	0.0128	0.4765	3, 4, 5
Mothra Field	0.11	19.50	25.00	0.16	2.75	4.88	0.0003	0.0084	0.0100	5
Axial seamount	0.86	1.00	2.95	10.93	41.00	53.00	0.0038	0.0498	0.1169	5
Middle Valley, Bent Hill	0.21	0.40	0.66	0.09	0.50	2.04	0.0020	0.0061	0.0130	6
Gorda Ridge										
Escanaba Trough	1.10	2.05	2.68	0.03	0.11	2.05	0.0018	0.0700	0.2425	7, 8, 9

(*continued on next page*)

Table 2 (*continued*)

Sites	Cu (wt%)			Zn (wt%)			Pb (wt%)			Ref.
	1st quartile	Median	3rd quartile	1st quartile	Median	3rd quartile	1st quartile	Median	3rd quartile	
East Pacific Rise										
21° N	0.79	1.45	6.78	0.63	2.65	19.55	0.0066	0.0214	0.0443	10, 11, 12
13° N	0.50	1.20	7.60	0.07	6.80	30.50	0.0139	0.0479	0.1640	10, 13
7° 24′ S	3.79	6.38	23.07	0.18	1.13	3.60	0.0123	0.0275	0.0568	14
16° 43′ S	1.53	8.50	14.75	0.85	3.73	11.50	0.0140	0.0300	0.0465	14
Galapagos Rift	1.88	4.99	7.35	0.25	1.35	3.12	0.0120	0.0206	0.0350	4, 5, 11, 15, 16, 17, 18, 19
Mid-Cayman Rise										
Beebe	0.31	1.41	4.72	0.09	0.26	4.46	0.0024	0.0119	0.0294	20
Mohns Ridge										
Loki's Castle	0.65	1.14	1.67	0.27	2.50	5.24	0.0080	0.0445	0.4658	21
Mid-Atlantic Ridge										
Semenov	0.09	0.33	14.20	0.05	0.07	9.42	0.0081	0.0207	0.0261	22, 23
Broken Spur	0.72	3.55	6.80	0.16	1.18	6.35	0.0008	0.0107	0.0491	5
Rainbow	–	18.17	–	–	2.59	–	–	0.0053	–	24, 25
Logatchev 1	10.98	30.00	33.98	0.07	0.07	1.45	0.0033	0.0033	0.0119	26
Peterburgskoe	1.96	3.58	6.52	0.04	0.05	0.09	0.0008	0.0054	0.0106	This work
Irinovskoe	1.55	19.90	28.80	0.10	0.16	0.41	0.0019	0.0039	0.0104	This work
TAG	0.52	2.02	14.7	0.215	7.6	51.5	0.0027	0.0160	0.0495	2, 4, 17, 27, 28, 29, 30, 31
Snakepit	0.80	1.89	3.66	0.19	0.66	3.14	0.0060	0.0200	0.0383	2, 4, 17
Krasnov	–	0.08	–	–	0.10	–	–	0.0071	–	This work
Southwest Indian Ridge										
Yuhuang-1	0.07	0.11	0.36	0.81	3.19	6.80	0.0051	0.0066	0.0086	32
Central Indian Ridge										
MESO Zone	0.52	3.98	15.29	0.06	0.13	0.18	0.0108	0.0181	0.0391	33, 34
Kairei	12.74	25.90	33.10	0.08	0.30	7.06	0.0003	0.0016	0.0270	35
Edmond	0.13	6.25	14.25	0.08	18.68	43.50	0.0260	0.0559	0.0852	36
GLOBAL	0.58	2.48	8.54	0.11	0.70	5.46	0.0041	0.0140	0.0371	

References: 1) Barrett et al. (1990); 2) Hannington et al. (1991b); 3) Samson (1986); 4) Geological Survey of Canada unpublished data; 5) TU Freiberg, unpublished data; 6) Ames et al. (1993); 7) Krasnov et al. (1995); 7) Koski et al. (1994); 8) Benninger and Koski (1987); 9) Koski et al. (1988); 10) Moss and Scott (1996); 11) Bischoff et al. (1983); 12) Zierenberg et al. (1984); 13) Geometep 3 Cruise Report; 14) Marchig et al. (1997); 15) Becker (1987); 16) GARIMAS II, 1987 Cruise Report; 17) Hannington (1989); 18) GARIMAS I, 1986 Cruise Report; 19) Embley et al. (1988); 20) Webber et al. (2015); 21) da Cruz (2015); 22) Melekestseva et al. (2014); 23) Melekestseva et al. (2017); 24) Marques et al. (2006); 25) Marques et al. (2007); 26) Murphy and Meyer (1998); 27) Hannington et al. (1995); 28) Tivey et al. (1995); 29) Petersen (2000); 30) Hannington et al. (1991a); 31) Rona et al. (1993); 32) Liao et al. (2018); 33) Halbach et al. (1996); 34) Halbach et al. (1998); 35) Wang et al. (2014); 36) Wu et al. (2016).

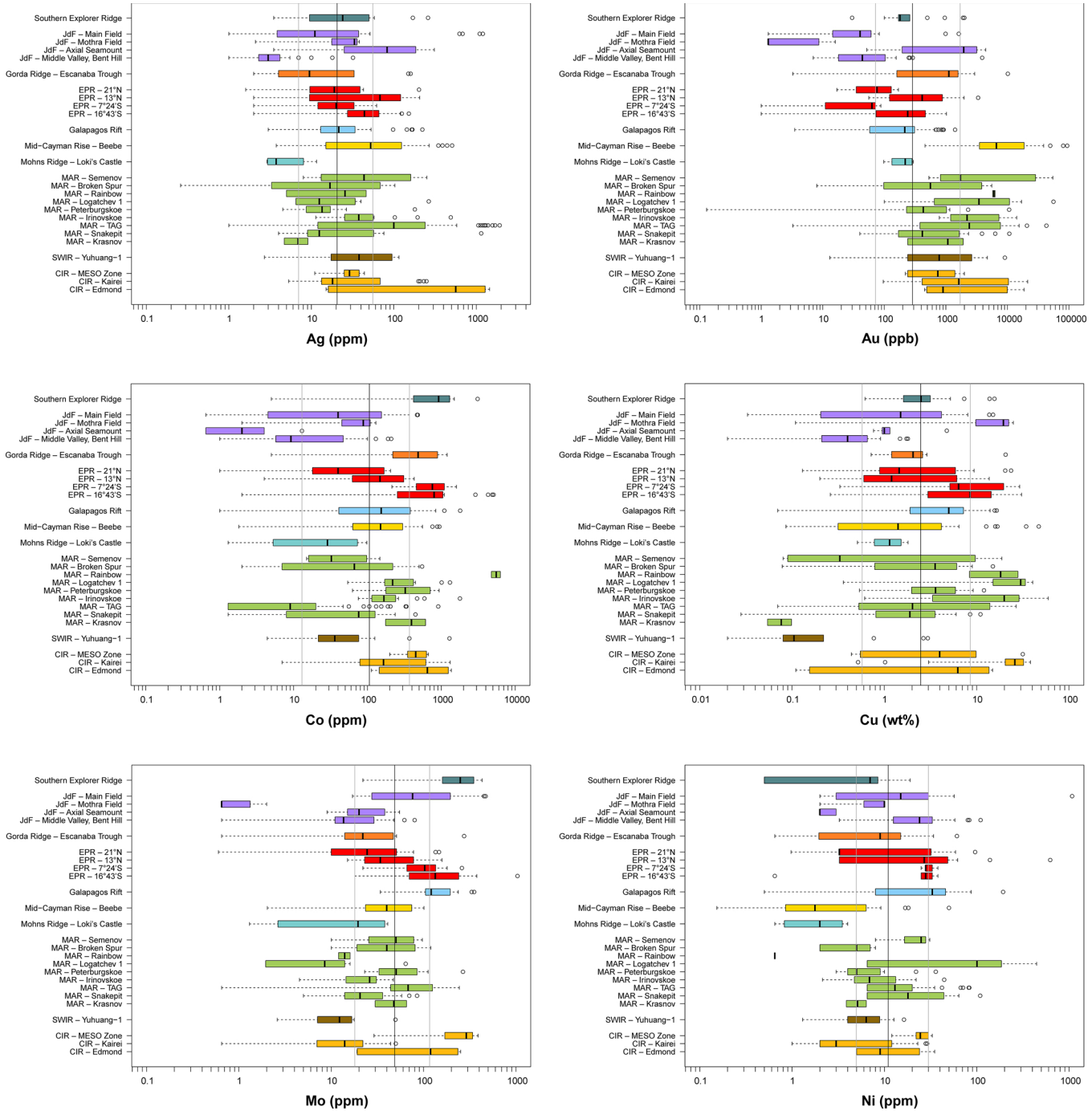

Fig. 1. Box-and-whiskers plots indicating the distribution of elements in the various sites. The boxes comprise the data between the first and third quartile (Q1 and Q3). The thick bar inside the boxes is the median, while the whiskers are calculated as Q1–1.5 × (Q3-Q1) and Q3 + 1.5 × (Q3-Q1). The circles represent the outliers. The three vertical lines (from left to right) represent the Q1, median and Q3 of the global distribution of the specific element (see Table 2 for the values).

3.2. Robust PCA and FA

The rPCA was used to determine the number of factors suitable to describe the compositional variability of the SMS deposits. The results of the rPCA are illustrated in the scree plot in Fig. 2 (see Fig. S1 for complete score plot). The line connecting the eigenvalues shows a progressive decrease in slope from PC1 to PC4 and only minor changes beyond PC3. Moreover, the first three components together explain most of the variability (~75%). For these reasons, three factors were chosen in the subsequent factorial analysis. As shown in Fig. 3, the most important variables in the first factor (F1) are Pb and Sb (plus minor contributions by Zn and Ag) with positive loadings and Cu and Se (Co) with negative loadings. The second factor (F2) is mainly related to Au and Ag (negative loadings) and more weakly affected by Mo, Se and Ni (positive loadings). The third factor (F3) is mostly influenced by Zn (Sb, Ag) (positive loadings) and Co (Mo) (negative loadings). The score plots in Fig. 4 show the distribution of the samples in the space defined by the factors. Fig. S2 shows the same results for individual sites. The samples are scattered through the plots, which indicates that rFA was effective in detecting the directions of maximum variability. Most remarkably, the F1 vs. F2 plot (Fig. 4A) shows that the factor F2 (Se-Mo-Ni vs. Au-Ag) discriminates well between SMS samples from (ultra)slow-spreading ridges (Mid-Atlantic Ridge, Mid-Cayman Rise, Southwest Indian Ridge, Central Indian Ridge) and those from intermediate/fast-

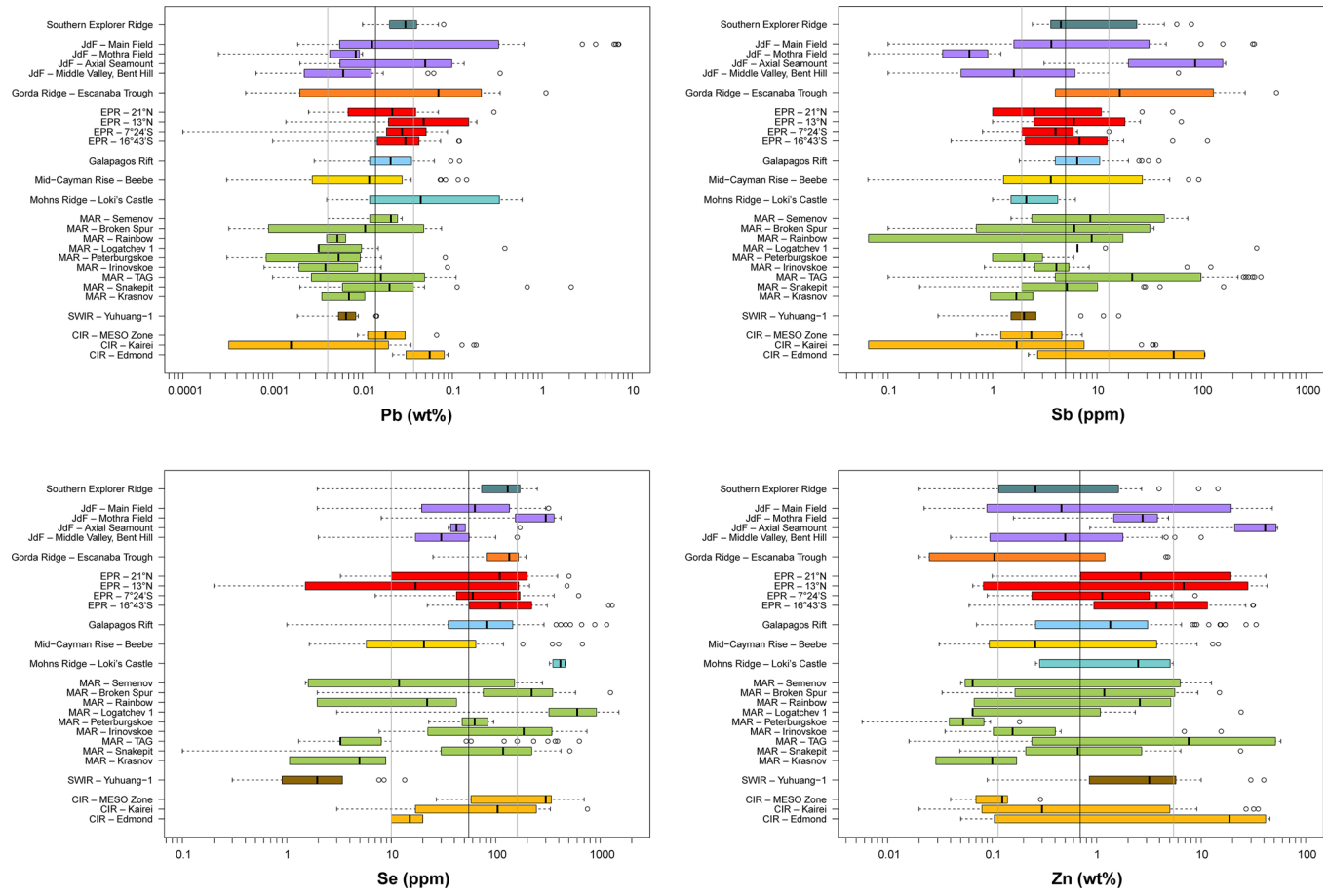

Fig. 1. (*continued*)

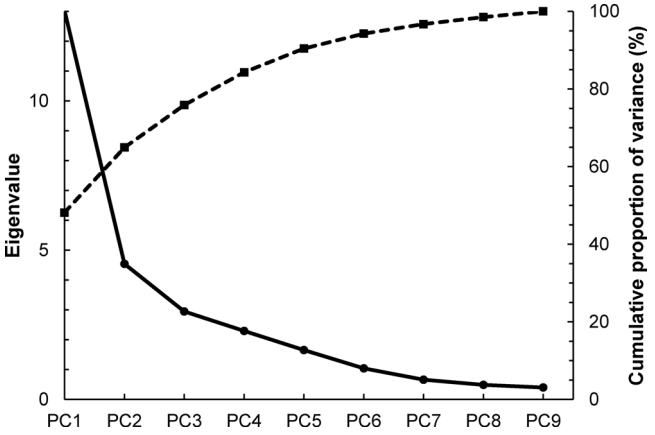

Fig. 2. Screeplot resulting from the robust PCA. The first three components describe the greatest proportion of variance.

spreading ridges (Southern Explorer Ridge, Juan de Fuca Ridge and Galapagos Rift). The great majority (87%) of the samples from intermediate/fast-spreading ridges show positive F2 loadings and only 7% of them show F2 loadings < -0.1. Most of these low-F2 samples are from the sedimented, intermediate-spreading Gorda Ridge (Escanaba Trough) and Juan de Fuca Ridge (Middle Valley) (Fig. S2A). The great majority (84%) of the samples from (ultra)slow-spreading ridges show negative F2 values and only 4% of them show F2 values $> +0.1$. No particular cluster is apparent in the F1 vs. F3 plot (Fig. 4B), although all but one samples from the Escanaba Trough and all samples from the mafic-hosted Petersbursgkoe field of the slow-spreading Mid Atlantic Ridge show more or less negative F3 scores (Fig. 4B and Fig. S2B). The F2 vs. F3 plot (Fig. S3) does not show any additional remarkable features and only confirms the good discrimination between SMS from intermediate/fast- and (ultra)slow-spreading ridges. Concerning samples from (ultra)slow-spreading ridges (low F2), the ultramafic-hosted SMS have, on average, lower values of F1 relative to the mafic-hosted SMS (Fig. 4A). Nonetheless, the ranges of factors F1, F2 and F3 covered by the two groups of samples are similar and no clear distinction between mafic- and ultramafic-hosted deposits is apparent in either plots (Fig. 4A,B). Since the ultramafic-hosted deposits are undersampled in our database ($N_{ultramafic} = 64$; $N_{mafic} = 362$), it may be argued that these results are biased due to the disproportionate weight of the mafic-hosted deposits. To test this possibility, we have performed rFA on a reduced data set in which the mafic records were randomly selected to match the number of the ultramafic records (Fig. S4). The resulting statistical factors F1 and F2 are very similar in terms of both element associations and relative factor weights to those obtained using the complete database (cf. Fig. 4). The discrimination between fast/intermediate-spreading and (ultra)slow-spreading ridges is somewhat less effective, probably due to the smaller number of input data, but there is still substantial overlap between ultramafic-hosted and mafic-hosted deposits from (ultra)slow-spreading ridges. This confirms the robustness of our rFA analysis.

3.3. Thermodynamic modeling

The complete results of thermodynamic modeling of basalt/seawater and peridotite/seawater reactions at 400 °C, 30 MPa, and log(r/w) ratios ranging between -5 and 0 are shown in Fig. S5 and Fig. S6. The most relevant results are summarized in Fig. 5. The first consequence of basalt/seawater and peridotite/seawater reactions is the development of alteration mineral assemblages, the nature of which in

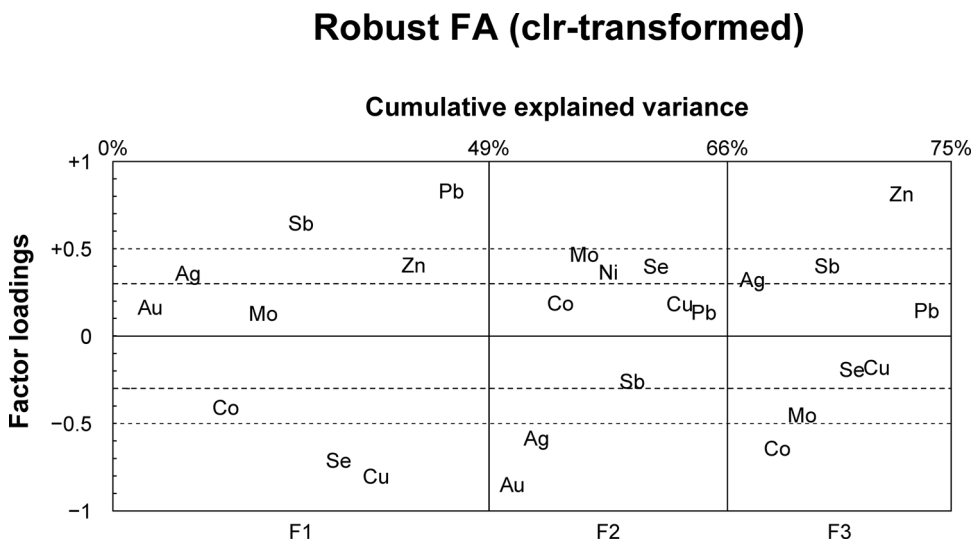

Fig. 3. Factor loading plots for the clr-transformed MS data. The variables (elements) that most significantly affect the factors have loadings > 0.5 (thin dashed lines). Variables with loadings < 0.3 (thick dashed lines) are almost irrelevant and those with loadings < 0.1 are not reported in the plot.

turn affects the composition of the hydrothermal fluid (Fig. S5 and S6).

In the basalt/seawater system, at very low log(r/w) (−5 to −3.1) the secondary mineral assemblage includes chrysotile, Mg chlorite, anhydrite, hematite, and titaniferous oxides, plus brucite at log(r/w) < −3.6 (Fig. 5A). Within this log(r/w) range, the seawater-buffered system is characterized by a high redox potential ($Eh_{400°C}$ ~ 0.2 V). The $pH_{400°C}$ values decrease from ~7.7 at log(r/w) –5 to ~6.3 at log(r/w) –3.1. With increasing log(r/w), the formation of abundant secondary silicates (talc, quartz, amesite, actinolite, Mg-Mn chlorite, epidote, albite) and chromite produces a jump in fluid $pH_{400°C}$ to ~6.7 and then a further progressive increase to ~7.4 at log(r/w) 0. At the same time, $Eh_{400°C}$ drops to −0.4 V at log(r/w) –3 and then further decreases to below −0.6 V (Fig. 5A). At log(r/w) > −1.8 hematite is replaced by magnetite. At log(r/w) > −1.3, when $Eh_{400°C}$ goes below ~ −0.6 V ($\log fO_2$ ~ −25), several sulfides are also formed (Fig. 5A). The computed alteration assemblages are consistent with natural and calculated assemblages in altered oceanic basalts (Alt et al., 1986; McCollom and Shock, 1998; Wetzel and Shock, 2000). Fig. 5A shows the calculated concentrations of several elements in the fluid as a function of the r/w ratio. The Fe and, in part, the Si contents are closely related to the Eh and pH values. The chalcophile elements accumulate in the fluid until their respective sulfides are stabilized in the altered rock, and then their concentrations in the fluid decrease. A subsequent minor increase of Co at log(r/w) > −0.3 is related to the disappearance of Co-bearing pyrite. The change in the Ni curve at log(r/w) –2.6 coincides with a change in the Ni contents of amesite, whereas that at log(r/w) –1.7 is related to the disappearance of Ni-bearing amesite. Formation of Ni-bearing sulfides at log(r/w) –1.2 produces a slight decrease in Ni concentrations to log(r/w) 0. Gold and Ag progressively accumulate in the fluid with increasing r/w ratios.

In the peridotite/seawater system, the secondary mineral assemblage is dominated by chrysotile at all r/w ratios (Fig. S6). At log(r/w) < −4 the seawater-buffered system is characterized by relatively high $Eh_{400°C}$ (~ 0.1 V) and $pH_{400°C}$ (~7.8). With increasing log(r/w), the stabilization of titaniferous oxides is accompanied by a slight decrease in pH to 6.8 at log(r/w) –2.6. With further increasing log(r/w), the pH variations are complicated due to the formation and disappearance of various secondary silicates (chlorite, phlogopite–biotite s.s., talc, actinolite) and show an overall increase, reaching a value of ~7.8 at log(r/w) 0. The $Eh_{400°C}$ values show a nearly flat profile to log(r/w) –3.3, then a marked drop to −0.5 V and a further decrease to below −0.8 V at log(r/w) 0 (Fig. 5B). Hematite is part of the alteration assemblage at log(r/w) < −2.5 and is replaced by magnetite at higher log(r/w). At log(r/w) > −2, when $Eh_{400°C}$ goes below −0.6 V ($\log fO_2$ ~ −25), several sulfides are also formed (Fig. 5B). The computed alteration assemblages are fairly consistent with natural and calculated assemblages in altered oceanic peridotites (Wetzel and Shock, 2000; Palandri and Reed, 2004; Klein and Bach, 2009; Klein et al., 2013). Element contents in the fluid follow broadly similar trends vs log(r/w) as in the basalt/seawater system (Fig. 5). Fe and Si contents are closely related to variations of Eh, pH and silicate mineralogy, Au and Ag progressively accumulate in the fluid, and the concentrations of the chalcophile elements increase until their respective sulfides are formed. The stabilization of (Co, Ni)-bearing sulfides occurs at somewhat lower log(r/w) than in the basalt/seawater system. The $Eh_{400°C}$ and fO_2 profiles are not strongly dissimilar in the two systems, except at log(r/w) ratios > − 0.5, where the peridotite/seawater system becomes more strongly reduced.

4. Discussion

4.1. The effect of temperature

Factor F1, which explains 49% of the variability, is dominated by the anti-correlated groups of elements Cu-Se-(Co) and Pb-Sb-(Zn-Ag) (Figs. 3 and 4). We interpret this anti-correlation to reflect variations in the formation temperature of the mineral assemblages analyzed. Because chalcopyrite solubility in vent fluids drops below 350–375 °C, higher temperature fluids precipitate chalcopyrite-rich (i.e., Cu-rich) assemblages, while lower temperature fluids precipitate Pb-Sb-bearing assemblages with variable proportions of galena and sulfosalts (Janecky and Seyfried, 1984; Seyfried and Ding, 1995). The strong correlation between Se and Cu reflects the ability of Se to replace S in high-temperature chalcopyrite (Huston et al., 1995). Cobalt, which as a divalent cation can substitute for Fe^{2+} and Zn^{2+}, can also be structurally hosted in chalcopyrite, as well as in high-temperature (> 300 °C) Fe-sulfides (Vaughan and Rosso, 2006; Cook et al., 2009; Grant et al., 2018). Galena and sulfosalts are often present only as (sub-)microscopic inclusions in low-temperature assemblages (e.g., Wohlgemuth-Ueberwasser et al., 2015; Grant et al., 2018) and may thus not have been reported in sample descriptions summarized in Table S1. Nonetheless, Grant et al. (2018) showed that significant concentrations of Pb, Ag and Sb in pyrite from relatively cold and distal parts of the TAG sulfide mound were in fact related to inclusions of galena and sulfosalts. The small positive loading of Zn in factor F1 is consistent with the tendency of sphalerite to precipitate at intermediate to low temperatures (T < ~300 °C;

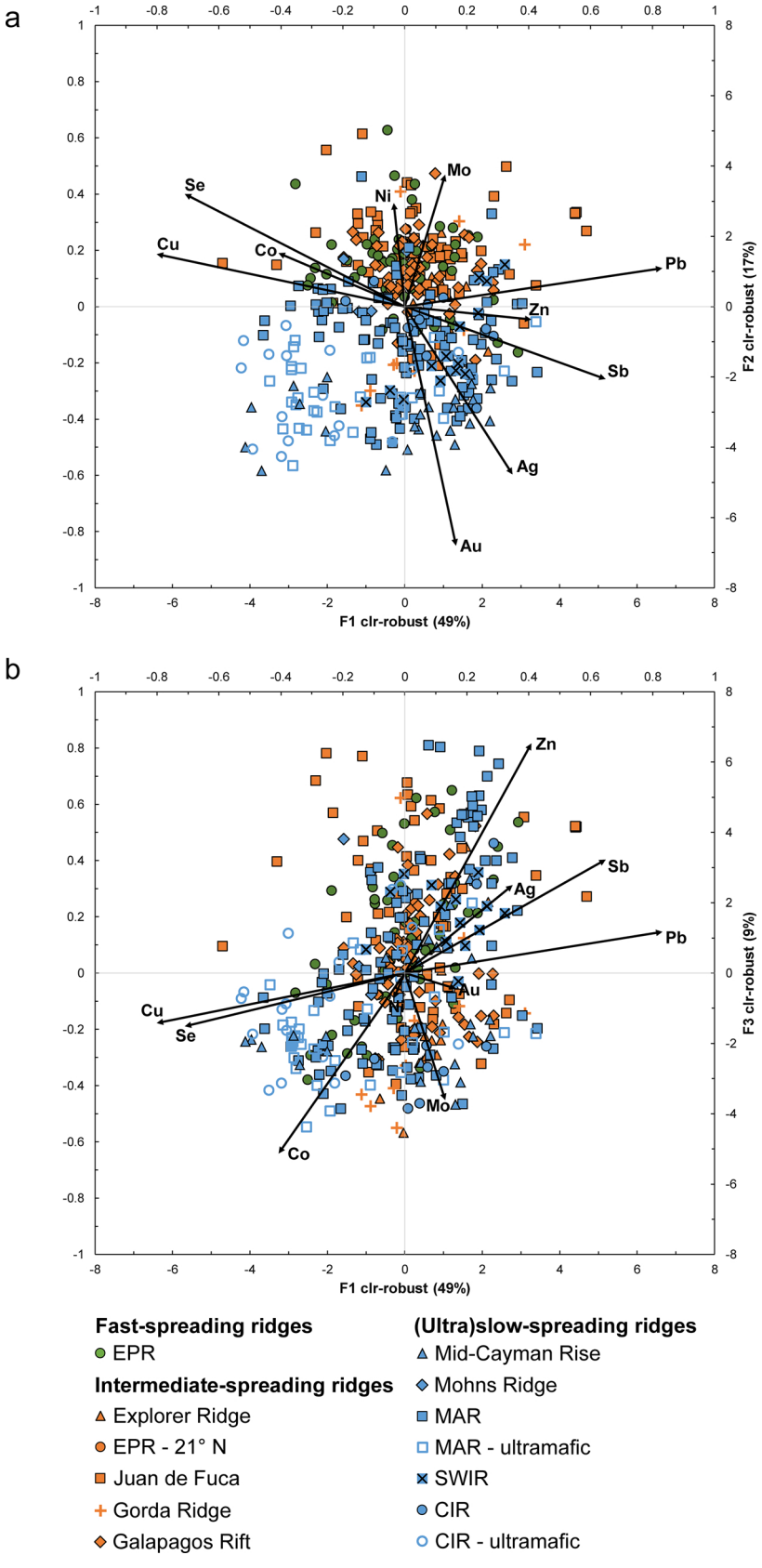

Fig. 4. Biplots for the robust FA of clr-transformed MS data: a) F1 vs. F2; b) F1 vs. F3. Lower horizontal and right axes refer to the coordinates of the data points (scores), while upper horizontal and left axes refer to the coordinates of the variables (loadings). Data for individual sites are illustrated in Fig. S2.

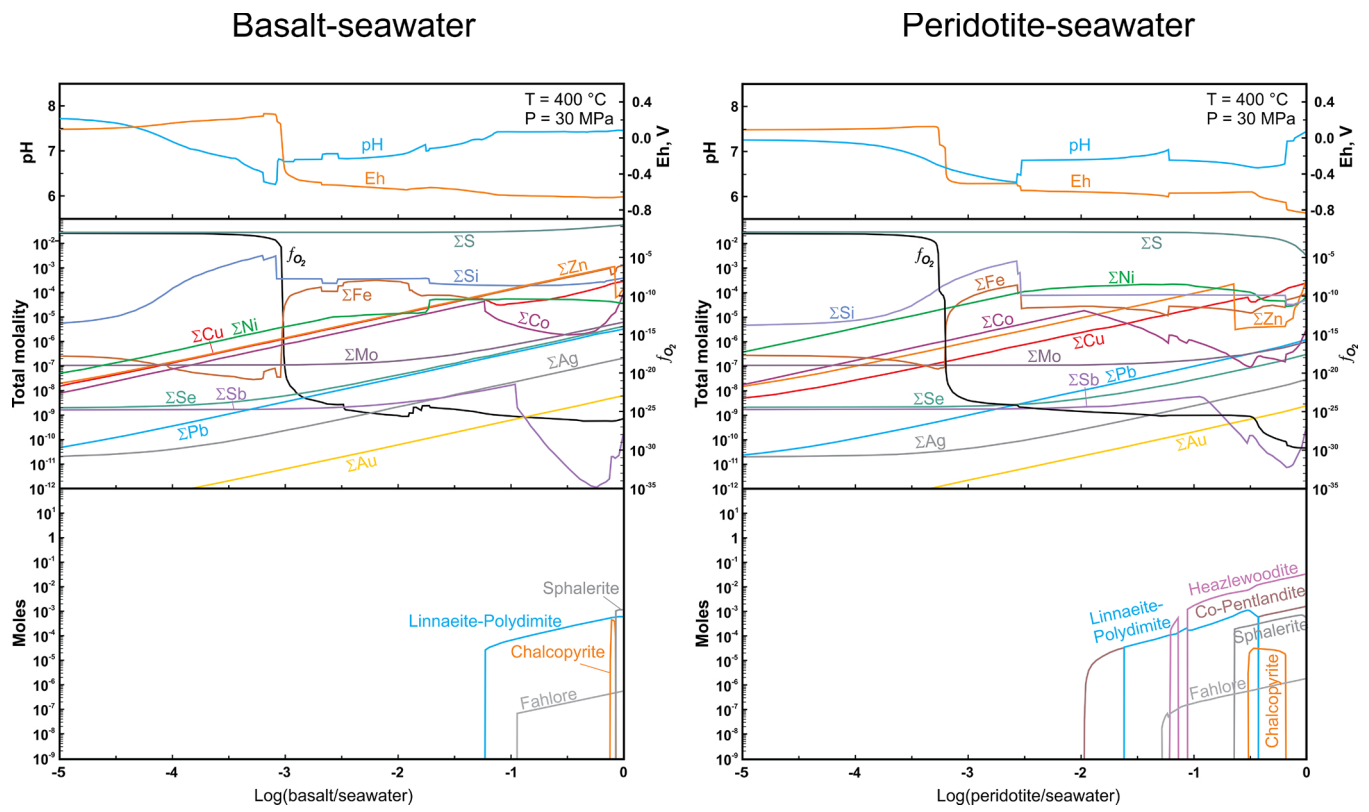

Fig. 5. Physicochemical model of the interaction of seawater with basalt (left) and peridotite (right) at various r/w ratios (see Table SM2 for the compositions of the reactants). The geochemical characteristics (pH, Eh, concentration of selected dissolved elements and fO_2) of the hydrothermal fluid are reported in the upper and middle boxes. Only secondary sulfides developed in the matrix of altered rocks are shown here (bottom boxes), since they greatly affect the concentration of dissolved metals (see Fig. S5 and Fig. S6 for complete mineralogical data). Note that the slight increase of Mo, and Se in solution at high r/w ratios is probably an artifact, since the model does not allow for their isomorphic incorporation in alteration minerals.

Janecky and Seyfried, 1984). The association of Sb with Pb and Zn may in part reflect substitution of Sb for Pb in galena (Sharp and Buseck, 1993) or for Zn in sphalerite (Maslennikov et al., 2017).

The depositional temperature is mostly controlled by conductive cooling of the hydrothermal fluids or mixing with cold seawater and can vary in time and space at the scales of individual hydrothermal fields (e.g., among different vents or as an effect of waning hydrothermal activity) and even samples (cf. the zonal structure of sulfide chimneys, showing chalcopyrite-rich inner portions formed at higher temperatures and pyrite-sphalerite-rich external portions formed at lower temperatures) (Hannington, 2014). This explains why samples from the same SMS deposit may plot at opposite ends with respect to factor F1 (Fig. S2). The tendency of samples from ultramafic-hosted SMS to show lower F1 loadings than mafic-hosted SMS from the same ridges may reflect the more diffuse high-temperature discharge and, thus, the widespread enrichment in high-temperature elements at the surface of these deposits (Fouquet et al., 2010).

4.2. The influence of ridge spreading rate

Factor F2, which explains 17% of the variability, provides a discrimination between Au-Ag-rich SMS from (ultra)slow-spreading ridges and Au-Ag-poor, but relatively Ni-Mo-Se-rich, SMS from intermediate/fast-spreading ridges (Fig. 4A). This is in line with the observation by Knight et al. (2018) that the Au content in seafloor SMS is negatively correlated with the ridge spreading rate. Knight et al. (2018) suggested several possible explanations for this geochemical distinction, including the intensity and duration of fluid-rock interaction, variations in the Au content in the source rocks and differences in fluid chemistry. Here we discuss the possible causes in the light of existing geochemical data and of our statistical analysis and geochemical modeling.

The composition of the substrate has been invoked as an important factor in controlling Au enrichment. However, the absolute average Au concentration in ultramafic rocks (0.49 ppb) is not much higher than that in mid-ocean ridge basalts (MORBs) (0.34 ppb) and is unlikely to determine a significant difference in the amount of Au dissolved in the hydrothermal fluids (Fouquet et al., 2010; Melekestseva et al., 2017; Fuchs et al., 2019). Thus, even assuming a metal contribution from ultramafic rocks for all Au-rich SMS from (ultra)slow-spreading ridges, the Au content in the substrate alone cannot explain their distinct geochemistry.

In our database, the samples with the lowest F2 scores are those from the ultramafic-hosted Irinovskoe, Kairei, Logatchev 1 and Rainbow sites and from the mafic-hosted Beebe and TAG sites. The fluids venting at Kairei, Logatchev 1 and Rainbow are relatively reduced (Kairei: $\log fO_{2,\ 350\ °C} \sim -31$ and $H_2 \sim 5$ mM; Logatchev 1: $\log fO_{2,\ 350\ °C} \sim -32.3$ and $H_2 \sim 12$ mM; Rainbow: $\log fO_{2,\ 350\ °C} \sim -33.6$ and $H_2 \sim 16$ mM; Charlou et al., 2002; Kumagai et al., 2008; Seyfried et al., 2011; Kawasumi and Chiba, 2017) and similar redox states are expected for fluids from Beebe as they have similar H_2 concentrations ($H_2 \sim 20$ mM; McDermott et al., 2018). Higher fO_2 are reported for TAG vent fluids ($\log fO_{2,\ 350\ °C} \sim -29$; $H_2 \sim 0.2$ mM; Charlou et al., 1996; Kawasumi and Chiba, 2017), which have a redox state within the range of vent fluids from other mafic-hosted sites on the East Pacific Rise ($\log fO_{2,\ 350\ °C} \sim -28$ to -29, $H_2 \sim 0.1$ mM, at 13° N; $\log fO_{2,\ 350\ °C} \sim -29$ to -31, $H_2 \sim 0.4$ mM, at 21° N; Tivey, 1995; Pester et al., 2011; Kawasumi and Chiba, 2017), Juan de Fuca ($\log fO_{2,\ 350\ °C} \sim -29$ to -30, $H_2 \sim 0.4$ mM, at Main Endeavour Field; Seewald et al., 2003; Kawasumi and Chiba, 2017) and Central Indian Ridge ($\log fO_{2,\ 350\ °C} \sim -28$ to -29, $H_2 \sim 0.2$ mM, at Edmond Hydrothermal Field; Gallant and Von Damm, 2006; Kumagai et al., 2008 Kawasumi and Chiba, 2017). Detailed data on fluid chemistry are not available for

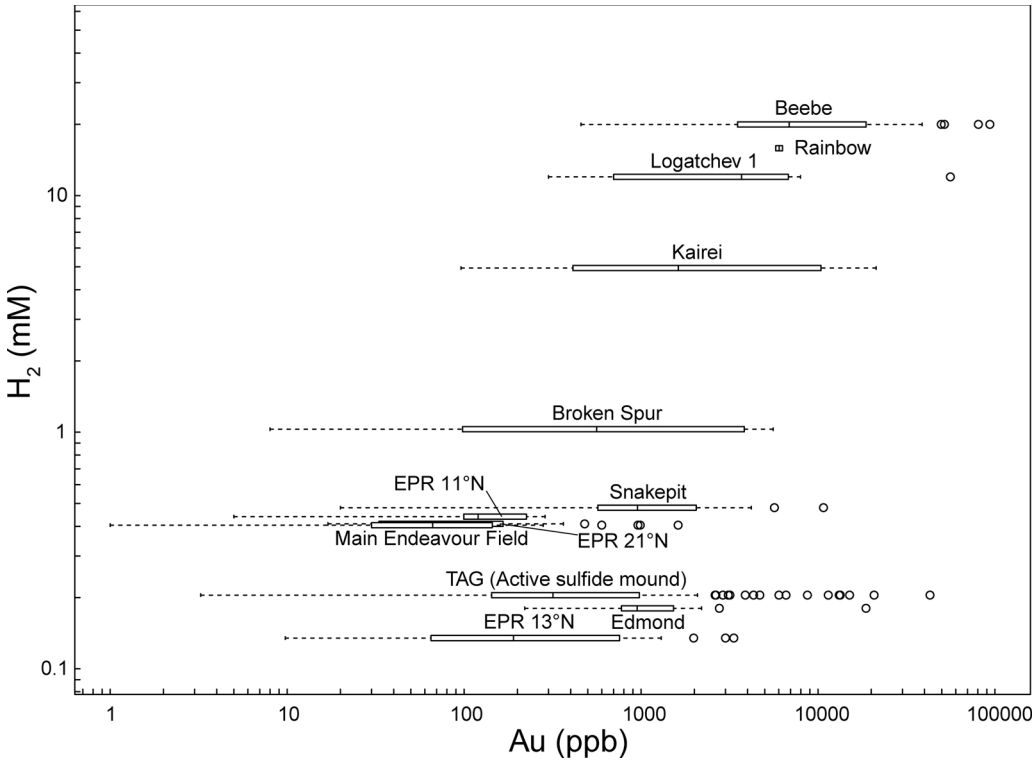

Fig. 6. Distribution of Au concentration in SMS vs. H_2 in vent fluids. The meaning of the boxes and whiskers is the same as in Fig. 1. Data for vent fluids after Campbell et al. (1988), Charlou et al. (1996, 2002), Kumagai et al. (2008), Fouquet et al. (2010), Gallant (2006), Jean-Baptiste et al. (1991), McDermott et al. (2018), Pester et al. (2011), Seewald et al. (2003), Seyfried et al. (2011), and Tivey et al. (1995). Data for SMS are compiled in Table S1.

Irinovskoe. A plot of Au vs. H_2 (Fig. 6) shows that the median Au concentration is generally higher in SMS from (ultra)slow-spreading ridges and that the highest values are observed at sites where the vent fluids are the most reduced, suggesting a genetic link between Au enrichment and fluid redox state. Note that the number of SMS samples with reported Au concentrations that could be plotted in Fig. 6 for the highly variable TAG is much larger than that included in the filtered database used for the multivariate rPCA and rFA (cf. Table 2 and S1), which justifies its relatively low median Au (Fig. 6) in spite of its relatively low F2 scores (Fig. 4). Fluids venting at sites with the highest Au and H_2 contents range from vapor-dominated (e.g., Beebe; McDermott et al., 2018) to seawater- (e.g., Logatchev; Charlou et al., 2002) or brine-dominated (e.g., Kairei and Rainbow; Charlou et al., 2002; Gallant, 2006). The variable chlorinities of fluids vented at sites characterized by similar Au endowment suggest that phase separation is not the primary factor in determining the overall Au enrichment.

The apparent correlation between Au enrichment and redox state must be considered cautiously. In fact, present-day vent fluid compositions may not be fully representative of a specific site, as vent fluid composition can considerably vary in time and space even within the same hydrothermal field (Lowell et al., 1995). This can partially explain why sulfide samples from TAG, for which the most comprehensive sample set is available, also show the largest compositional variability (Fig. 6). More generally, relations based on absolute element concentrations are unavoidably affected by sampling bias. More robust information can be obtained by considering the geochemical relations of Au with other elements and particularly with those having large positive or negative loadings in factor F2 (i.e., Ni, Mo, Se, and Ag).

In the oceanic lithosphere, Ni, Mo, Se, Au, and Ag are typically stored in sulfides (Patten et al., 2016; Holwell et al., 2017). Therefore, the presence of these elements in seafloor hydrothermal fluids is strictly related to alteration and re-precipitation of sulfides in the substrate rocks. A high temperature in the reaction zone may enhance Au (and H_2) concentrations in the fluid (McDermott et al., 2018), but it would also increase Ni solubility (Liu et al., 2012). Therefore, reaction temperature cannot explain factor F2, in which Au and Ni are anti-correlated (Figs. 3 and 4). Fuchs et al. (2019) showed that, in ultramafic-dominated systems, strongly reduced hydrothermal fluids such as those produced by peridotite serpentinization promote the deposition of Au at relatively high temperatures. This may support a link between fluid redox state and Au endowment (cf. Fig. 6). However, the similar F2 scores shown by mafic- and ultramafic-hosted SMS from (ultra)slow-spreading ridges (Fig. 4A) suggest that Au enrichment and redox conditions may be largely independent of seafloor substrate composition. Thermodynamic modeling of basalt–seawater and peridotite–seawater reactions shows that, at a given temperature, the concentrations of metals in the fluid are chiefly controlled by r/w ratios and sulfide solubility (Fig. 5). At low r/w ratios, relatively oxidized seawater-dominated fluids favor sulfide dissolution (Palandri and Reed, 2004; Liu et al., 2012; Holwell et al., 2017; Melekestseva et al., 2017). The enrichment in Ni relative to Au and Ag in SMS deposits from intermediate/fast-spreading ridges may thus be an effect of the enhanced dissolution of Ni-rich magmatic sulfides. Higher r/w ratios, which should be more typical of slow-spreading ridges, would instead stabilize sulfides that may segregate Ni while the concentrations of dissolved Au and Ag progressively increase (Fig. 5; see also Melekestseva et al., 2017). High r/w ratios can potentially also be achieved in reaction zones beneath sedimented ridges, where the low-porosity sediment cover may limit seawater fluxes through the oceanic crust. This may explain why most of the samples from the intermediate-spreading, but sedimented, Gorda and Juan de Fuca ridges have low F2 scores similar to samples from (ultra)slow-spreading ridges (Fig. 4A). Several other elements, which, based on thermodynamic modeling, should also be sensitive to r/w ratios (Fig. 5), do not appear to be controlled by factor F2 (Pb, Sb, Cu, Zn, Co) or have small F2 loadings (< 0.5) which are opposite in sign to expectations (Se, Mo). This apparent inconsistency can be explained by the fact that most of these elements are more strongly controlled by other factors, such as depositional temperature (Pb, Sb, Cu, Se, Co) and zone refining processes (Zn, Co; see below). Therefore, the influence of r/w ratio on these elements may not be apparent in factor F2. As for Mo and Se, their model concentrations at high r/w ratios (Fig. 5) are probably overestimated, because the model does not allow for their incorporation in alteration silicates and sulfides, which may contain significant traces of these elements

(Wedepohl, 1969). Expecting an enrichment in these elements at high r/w ratios is therefore unwarranted. Our thermodynamic models do not consider possible kinetic effects, which may strongly influence fluid chemistry in ultramafic-hosted systems at high temperature (Allen, 2003). However, they suggest a possible mechanism for (Au, Ag)–Ni decoupling, which may be effective at least under near-equilibrium conditions in both mafic and ultramafic substrates.

It is noteworthy that in both basalt–seawater and peridotite–seawater systems, fO_2 is predicted to decrease at high r/w ratios as a consequence of alteration of ferrous Fe-bearing silicates (Fig. 5). Thus, the association between high dissolved H_2, negative F2 loading and high Au grade in many hydrothermal sites on (ultra)slow-spreading ridges (Figs. 4A and 6) may at least in part be a consequence of reactions between seawater and substrate rocks at relatively high r/w ratios rather than of reactions of seawater with specific lithologies. The dispersion of F2 values for both (ultra)slow- and intermediate/fast-spreading ridges (Fig. 4A) reveals intra-ridge or even within-site geochemical variations, which can be ascribed to minor changes in space and time of hydrothermal circuits and r/w ratios. A similar interpretation was proposed by Bach and Humphris (1999) to explain variations in Sr and O isotope compositions of seafloor hydrothermal fluids.

Based on the results of thermodynamic modeling at 400 °C, the r/w ratios that would be the most significant in determining the observed compositional variability range from ~0.002 to 1, i.e., from log(r/w) –2.7 to log(r/w) 0 (Fig. 5). Within this range, a steady increase of dissolved Au and Ag is accompanied by constant or even decreasing Ni concentrations due to its incorporation into secondary silicates and sulfides. This range is compatible with the r/w ratios < 1 to < < 1 estimated for seafloor hydrothermal systems from experiments on hydrothermal alteration of seafloor rocks (Seyfried et al., 1988). Note that our r/w ratios refer to conditions in the reaction zone and thus are not directly comparable with the 'integrated' ratios calculated from geochemical data on vent fluids (B and Sr isotopes, Li/Cl ratios) and from geophysical data, which suggest a typical range of ~0.3–2 (Mottl, 2003; Seyfried Jr. and Shanks, 2004; Barker et al., 2010).

4.3. The effect of zone refining

Factor F3 explains 9% of the variability and discriminates Zn-rich, Co-Mo-poor assemblages from those that are poor in Zn but relatively enriched in Co and Mo (Figs. 3 and 4B). We interpret this anti-correlation to be related to zone refining processes. During zone refining, mixing of hydrothermal fluid with seawater within the sulfide mound leads to dissolution of earlier Zn-sulfides and precipitation of pyrite, anhydrite and chalcopyrite, producing moderate temperature fluids enriched in Zn (and Au, Ag, Sb, Pb, and Cd). These fluids may vent from white smokers, in which abundant sphalerite is re-precipitated (Edmond et al., 1995; Tivey et al., 1995; Hannington, 2014). Consistently, samples of white smoker chimneys from TAG show high F3 scores (Fig. S2). Cobalt and, especially, Mo are mainly stored in Fe sulfides, and pyrite in particular (up to several thousand or several hundred ppm, respectively; Maslennikov et al., 2009; Keith et al., 2016). Chalcopyrite can also host significant Co (up to several thousand ppm; Maslennikov et al., 2017). Therefore, Co and Mo are likely to remain relatively immobile during zone refining and, consistently, they show negative F3 scores. On the contrary, Ag and Sb, which have small positive loadings in F3, can have high concentrations in sphalerite (hundreds or tens of ppm respectively; Wang et al., 2018) and may be significantly remobilized and, eventually, re-concentrated in newly formed sphalerite near the mound surface. In fact, sphalerite from TAG white smokers have high concentrations of both Ag and Sb (up to > 1000 ppm and several hundred ppm, respectively; Tivey et al., 1995). Thus, F3 is likely to represent the effect of metal remobilization on the geochemistry of the hydrothermal fluid.

The relatively Zn-rich compositions of some samples from the Main Field on the Juan de Fuca Ridge, which fall in the upper left quadrant in Fig. 4B at high F1 and F3 loadings, may have a different origin. They have been ascribed to precipitation from relatively high-temperature but (Cu, Co)-depleted fluids, characterized by a pH higher than typical black smokers due to anomalously high concentrations of ammonia, possibly reflecting hidden organic-rich sedimentary rocks at depth (Tivey et al., 1999). These fluids precipitate Cu-Fe sulfides and then abundant Zn sulfides on conductive cooling within diffusely venting structures. This particular scenario may have produced geochemical associations in the final SMS deposit that are partly similar to those determined by zone refining at other sites.

4.4. The role of phase separation, magmatic input and substrate composition

The results of our statistical analysis can be explained by factors such as temperature of deposition, ridge spreading rate and varying r/w ratios in the reaction zone, and metal remobilization. If our interpretation is correct, then processes such as phase separation and the input of magmatic fluids, which have sometimes been invoked to explain the compositions of seafloor vent fluids and hydrothermal precipitates (Douville et al., 2002; Melekestseva et al., 2014, 2017; Tivey, 2007), do not play a major role in determining the overall geochemical variability of SMS on mid-ocean ridges. However, this does not mean that these processes do not occur.

Phase separation is believed to be commonplace in seafloor hydrothermal systems (Coumou et al., 2009). On mid-ocean ridges, it may give rise to vent fluids with different chlorinities and absolute metal contents (Charlou et al., 2002; Hannington et al., 2005; Fouquet et al., 2010; Seyfried et al., 2011). However, experimental studies show that element fractionation due to phase separation strongly depends on sulfur and chloride concentrations (Nagaseki and Hayashi, 2008; Pokrovski et al., 2005, 2008) and will be predictably small at the concentrations typical of seafloor vent fluids (H_2S: 0.5–13 mM, Cl^-: 420–950 mM; Fouquet et al., 2010; Kawasumi and Chiba, 2017). Thus, although in seafloor hydrothermal systems phase separation may certainly influence the absolute concentrations of metals in the fluids, their fractionation between vapor and liquid phases may not be such as to determine significant changes in the final metal-to-metal ratios, which mainly remain controlled by other higher-order factors.

A magmatic fluid input has been specifically invoked to explain the unusual characteristics of some SMS deposits at mid-ocean ridges, such as an anomalous abundance of barite or of silica and Au-Ag (Melekestseva et al., 2014, 2017). Our results are not inconsistent with this explanation. First, barite-rich samples were intentionally discarded in the present work. Second, our statistical analysis is sensitive to overall statistical trends, but does not discriminate outliers. Therefore, contributions from magmatic fluids that were significant only on a local scale could not be resolved.

One of the most intriguing and unexpected results of this work is that the composition of the substrate does not emerge as a primary factor in determining metal associations in SMS at mid-ocean ridges. We do not deny a possible role of the substrate in producing specific compositional features, but we suggest that, at a global scale, other factors may explain a large proportion of the observed geochemical variability. The fact that ultramafic substrates are restricted to (ultra) slow-spreading ridges may have obscured the role of spreading rate and r/w ratios in many previous evaluations. This may have led to potentially circular arguments, in which the occurrence of particular geochemical features, believed to be ultramafic- (or mafic-) related, in a mafic- (or ultramafic-) hosted deposit were ascribed to the involvement of concealed ultramafic (or mafic) rocks at depth (Marques et al., 2006; Wang et al., 2014; Webber et al., 2015). Some of these features might actually be more strongly related to the r/w ratios and, hence, to the ridge spreading rate.

For instance, it has been argued that the Co/Ni ratio of SMS can be

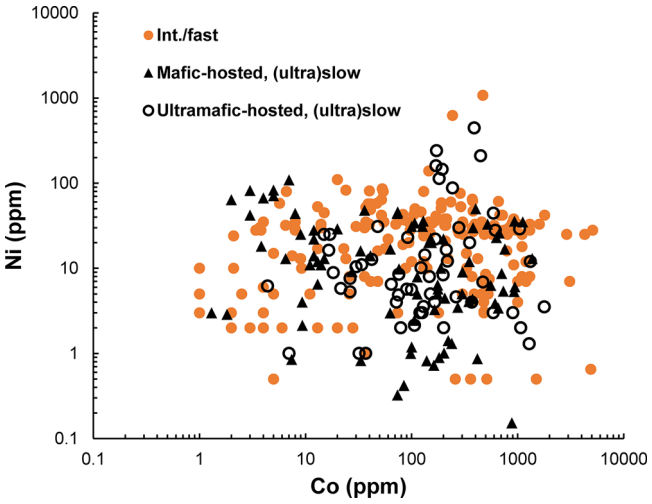

Fig. 7. Cobalt vs. Ni concentrations in SMS from intermediate/fast-spreading ridges and (ultra)slow-spreading ridges, distinguished between MORB- and ultramafic-hosted. Low-detects are not reported.

used to discriminate between mafic-dominated and ultramafic-dominated hydrothermal systems (Marques et al., 2006; Zaccarini and Garuti, 2008; Melekestseva et al., 2013). This hypothesis is consistent with the fact that the Co/Ni ratio is significantly higher in MORBs than in ultramafic rocks (0.35 vs. 0.05, calculated from data compiled in Fouquet et al., 2010). Fig. 7 shows the relationships between Ni and Co in mafic- and ultramafic-hosted SMS deposits from (ultra)slow- and intermediate/fast-spreading ridges. The various groups overlap significantly. Thus, although the nature of the substrate [mafic on intermediate/fast-spreading ridges and mafic and ultramafic on (ultra)slow-spreading ridges] is likely to exert some control on the distribution of Ni and Co in SMS deposits, the Co/Ni ratio overall appears to have little discriminatory power. This suggests that other factors, namely, depositional temperature, r/w ratios in the reaction zone, and zone refining, which may influence to various extent the concentrations of Co and Ni (i.e., F1, F2 and F3 in Fig. 4), may mask the effects of substrate composition when explored through a simple bivariate plot. However, the Co/Ni ratio may be more sensitive in the case of subseafloor stockwork and replacive mineralization, where the local contribution of Ni from ultramafic host-rocks may be significant (cf. Marques et al., 2007). This type of mineralization is not the focus of this work and was in fact excluded from our analysis.

Selenium has also been suggested as a potential ultramafic marker based on its higher average content in ultramafic-hosted SMS (Melekestseva et al., 2017), but the ranges of Se concentrations are similar for the mafic- and the ultramafic-hosted deposits (Fuchs et al., 2019). Based on our statistical analysis, Se is strongly related to factor F1, i.e., to the temperature of deposition (Fig. 4). Similar to what suggested by Fouquet et al. (2010) for Cu, the higher average content of Se in sampled ultramafic-hosted SMS may reflect the more diffuse high-temperature discharge and, thus, the widespread enrichment in high-temperature elements at the surface of these deposits.

Other features that seem to be typical of ultramafic-hosted SMS cannot be easily explained by factors F1, F2 and F3 and, therefore, have good potential as ultramafic markers. For instance, the median Au/Ag ratio in ultramafic-hosted SMS is five times higher than that in mafic-hosted SMS [$(Au/Ag)_{ultramafic}$ = 0.072; $(Au/Ag)_{mafic}$ = 0.015], in analogy with Au/Ag in ultramafic rocks vs. MORBs [$(Au/Ag)_{ultramafics}$ ~ 0.20; $(Au/Ag)_{MORB}$ ~ 0.020; Anderson, 1989]. The higher Au/Ag in ultramafic-hosted SMS may also reflect the lower pH of fluids produced during peridotite alteration (Fig. 5; see also Allen and Seyfried, 2003), which enhances Ag solubility in the cooling fluid (Fuchs et al., 2019). Another potential marker is Sn, which is systematically enriched in ultramafic-hosted SMS (Fouquet et al., 2010; Evrard et al., 2015; Melekestseva et al., 2017). Because of the scarcity of data for Sn, this element could not be included in our statistical analysis and its significance remains uncertain.

Another possibility that would be worth considering is that the fluids that formed *all* SMS deposits on (ultra)slow-spreading ridges interacted with both mafic and ultramafic rocks at depth. This scenario would explain the geochemical similarity between several mafic-hosted and ultramafic-hosted SMS deposits. However, the relative importance of ultramafic rocks vs. r/w ratios in determining the observed geochemical associations would remain difficult to resolve, as these factors are likely to be highly correlated with each other and with the ridge spreading rate.

5. Conclusions

The geochemical associations observed in SMS deposits on mid-ocean ridges can be explained by a combination of the following independent factors, given in order of importance: (1) temperature of deposition, (2) ridge spreading rate and (3) zone refining. The first and the third factors are mostly related to processes that operate near the seafloor, such as conductive cooling and/or mixing with seawater and metal remobilization, and determine the relative proportions of the main minerals and, thus, of Cu and Zn (Co, Se, Sb, Pb). Thus, they are mostly controlled by final depositional conditions and evolution of mound and vent structures rather than by the original geochemistry of the hydrothermal fluid. The ridge spreading rate directly influences the structure of the oceanic lithosphere, which in turn exerts a major control on the length and depth of the hydrothermal circuit and on the r/w ratios in the reaction zone, and thus on the behavior of precious metals and Ni (Mo, Se). Despite the obvious role played by substrate rocks in releasing elements to hydrothermal fluids, their nature (specifically mafic vs. ultramafic) does not clearly emerge as a statistically significant independent factor. Therefore, using simple parameters such as metal grades or bivariate metal ratios to discriminate between mafic and ultramafic hydrothermal systems may lead to erroneous evaluations. In any case, the relative importance of highly correlated factors such as r/w and ultramafic/mafic volume ratios in the reaction zone may be difficult to resolve using simple compositional data. The composition of the substrate, however, may become relevant in subseafloor mineralization, where sulfides precipitate by reaction of ascending hydrothermal fluids with substrate host-rocks. On a global scale, widely recognized processes such as phase separation and magmatic fluid input do not appear to play a major role in determining the overall geochemical diversity of SMS deposits on mid-ocean ridges. These processes may nevertheless have a significant influence on a small time-space scale, and may rather be reflected by peculiar mineral assemblages (e.g., barite-rich or silica and Au-rich), which are only found at specific sites.

Declarations of Competing Interest

None

Acknowledgments

This work is part of L.T.'s post-doctoral project at the Università di Padova. G.A.T. and I.Yu.M acknowledge financial support by the South Urals Federal Research Center, Urals Branch of Russian Academy of Sciences, Institute of Mineralogy, Miass, Russia (grant number AAAA-A-19-119061790049-3). The authors are grateful to the crew of *R/V Professor Logatchev* (Polar Marine Geosurvey Expedition, Lomonosov-St. Petersburg) for sampling the Irinovskoe, Krasnov and Peterburgskoe SMS fields. We are grateful to T. Monecke and two anonymous reviewers for their careful reading and constructive comments, which helped us to improve the manuscript.

Appendix A. Supplementary data

Supplementary data associated with this article can be found, in the online version, at http://dx.doi.org/10.1016/j.earscirev.2019.102958.

References

Allen, D.E., Seyfried Jr., W.E., 2003. Compositional controls on vent fluids from ultramafic-hosted hydrothermal systems at mid-ocean ridges: an experimental study at 400°C, 500 bars. Geochim. Cosmochim. Acta 67, 1531–1542.

Alt, J.C., Honnorez, J., Laverne, C., Emmermann, R., 1986. Hydrothermal alteration of a 1 km section through the upper oceanic crust, Deep Sea Drilling Project hole 504B: Mineralogy, chemistry, and evolution of seawater-basalt interactions. J. Geophys. Res. 91, 10309–10335.

Ames, D.E., Franklin, J.M., Hannington, M.D., 1993. Mineralogy and geochemistry of active and inactive chimneys and massive sulfide, Middle Valley, northern Juan de Fuca Ridge; an evolving hydrothermal system. Can. Mineral. 31, 997–1024.

Anderson, D.L., 1989. Composition of the Earth. Science 243, 367–370.

Bach, W., Humphris, S.E., 1999. Relationship between the Sr and O isotope compositions of hydrothermal fluids and the spreading and magma-supply rates at oceanic spreading centers. Geology 27, 1067–1070.

Barker, A.K., Coogan, L.A., Gillis, K.M., 2010. Insights into the behavior of sulphur in mid-ocean ridge axial hydrothermal systems from the composition of the sheeted dyke complex at Pito Deep. Chem. Geol. 275, 105–115.

Barrett, T.J., Jarvis, I., Jarvis, K.E., 1990. Rare earth element geochemistry of massive sulfides-sulfates and gossans on the Southern Explorer Ridge. Geology 18, 583–586.

Becker, K.P., 1987. *Die massiven sulfiderze des Galapagos Rifts mineralogisch-geochemische untersuchungen*, (Unpublished M. Sc. thesis). Institut für Mineralogie und Lagerstättenlehre, RWTH Aachen Germany, 105.

Benninger, L.M., Koski, R.A., 1987. Descriptions and Chemical Analyses of Sulfide Samples Dredged in 1986 from Escanaba Trough, Southern Gorda Ridge (No. 87-375-B). US Geological Survey.

Bischoff, J.L., Rosenbauer, R.J., Aruscavage, P.J., Baedecker, P.A., Crock, J.G., 1983. Sea-floor massive sulfide deposits from 21° N East Pacific Rise, Juan de Fuca Ridge, and Galapagos Rift; bulk chemical composition and economic implications. Econ. Geol. 78, 1711–1720.

Bougault, H., Charlou, J.L., Fouquet, Y., Needham, H., Vaslet, N., Appriou, P., Jean Baptiste, P., Rona, P.A., Dmitriev, L., Silantiev, S., 1993. Fast and slow spreading ridges: structure and hydrothermal activity, ultramafic topographic highs, and CH_4 output. J. Geophys. Res. Solid Earth 98, 9643–9651.

Campbell, A.C., Palmer, M.R., Klinkhammer, G.P., Bowers, T.S., Edmond, J.M., Lawrence, J.R., Casey, J.F., Thompson, G., Humphris, S., Rona, P., Karson, J.A., 1988. Chemistry of hot springs on the Mid-Atlantic Ridge. Nature 335, 514–519.

Charlou, J.L., Donval, J.P., Jean-Baptiste, P., Dapoigny, A., Rona, P.A., 1996. Gases and helium isotopes in high temperature solutions samples before and after ODP Leg 158 drilling at TAG hydrothermal field (26°N,MAR). Geophys. Res. Lett. 23, 3491–3494.

Charlou, J.L., Donval, J.P., Fouquet, Y., Jean-Baptiste, P., Holm, N., 2002. Geochemistry of high H_2 and CH_4 vent fluids issuing from ultramafic rocks at the Rainbow hydrothermal field (36 14′ N, MAR). Chem. Geol. 191, 345–359.

Chudnenko, K.V., 2010. Thermodynamic Modeling in Geochemistry: Theory, Algorithms, Software, and Applications. (Geo, Novosibirsk, 287 pp. [in Russian).

Cook, N.J., Ciobanu, C.L., Pring, A., Skinner, W., Shimizu, M., Danyushevsky, L., Saini-Eidukat, B., Melcher, F., 2009. Trace and minor elements in sphalerite: a LA-IC-MS study. Geochim. Cosmochim. Acta 73, 4761–4791.

Coumou, D., Driesner, T., Heinrich, C.A., 2008. The structure and dynamics of mid-ocean ridge hydrothermal systems. Science 321, 1825–1828.

Coumou, D., Driesner, T., Weis, P., Heinrich, C.A., 2009. Phase separation, brine formation, and salinity variation at Black Smoker hydrothermal systems. J. Geophys. Res. Solid Earth 114 (B03212).

da Cruz, M.I.F.S., 2015. *Mineralogy and Geochemistry of Contrasting Hydrothermal Systems on the Arctic Mid Ocean Ridge (AMOR): the Jan Mayen and Loki's Castle vent fields* (PhD thesis). Universidade de Lisboa, Portugal, (257).

Douville, E., Charlou, J.-L., Oelkers, E.H., Bienvenu, P., Colon, C.F.J., Donval, J.P., Fouquet, Y., Prieur, D., Appriou, P., 2002. The Rainbow vent fluid (36°14′N, MAR): the influence of ultramafic rocks and phase separation on trace metal content in Mid-Atlantic Ridge hydrothermal fluids. Chem. Geol. 184, 37–48.

Edmond, J.M.A., Campbell, C., Palmer, M.R., German, C.R., Klinkhammer, G.P., Edmonds, H.N., Elderfield, H., Thompson, G., Rona, P., 1995. Time series studies of vent fluids from the TAG and MARK sites (1986, 1990) Mid-Atlantic Ridge and a mechanism for Cu/Zn zonation in massive sulphide orebodies. In: Parson, L.M., Walker, C.L., Dixon, D.R. (Eds.), Hydrothermal Vents and Processes. Geol. Soc. Lond., Spec. Publ. 87, 77–86.

Embley, R.W., Jonasson, I.R., Perfit, M.R., Franklin, J.M., Tivey, M.A., Malahoff, A., Smith, M.F., Francis, T.J.G., 1988. Submersible investigation of an extinct hydrothermal system on the Galapagos Ridge; sulfide mounds, stockwork zone, and differentiated lavas. Can. Mineral. 26, 517–539.

Evrard, C., Fouquet, Y., Moelo, Y., Rinnert, E., Etoubleau, J., Langlade, J.A., 2015. Tin concentration in hydrothermal sulfides related to ultramafic rocks along the Mid-Atlantic Ridge: a mineralogical study. Eur. J. Mineral. 27, 627–638.

Filzmoser, P., Hron, K., 2011. Robust statistical analysis. In: Pawlowsky-Glahn, V., Buccianti, A. (Eds.), Compositional Data Analysis. Theory and Applications. John Wiley & Sons, Chichester (UK), pp. 59–72.

Filzmoser, P., Hron, K., Reimann, C., Garrett, R., 2009a. Robust factor analysis for compositional data. Comput. Geosci. 35, 1854–1861.

Filzmoser, P., Hron, K., Reimann, C., 2009b. Principal component analysis for compositional data with outliers. Environmetrics 20, 621–632.

Fouquet, Y., Cambon, P., Etoubleau, J., Charlou, J.L., Ondréas, H., Barriga, F.J., Cherkashov, G., Semkova, T., Poroshina, I., Bohn, M., Donval, J.P., Henry, K., Murphy, P., Rouxel, O., 2010. Geodiversity of hydrothermal processes along the Mid-Atlantic Ridge and ultramafic-hosted mineralization: a new type of oceanic Cu-Zn-Co-Au volcanogenic massive sulfide deposit. In: In: Rona, P.A., Devey, C.W., Dyment, J., Murton, B.J. (Eds.), Diversity of Hydrothermal Systems on Slow Spreading Ocean Ridges. Geophysical Monograph, vol. 188. American Geophysical Union, Washington DC, pp. 321–367.

Francheteau, J., Needham, H.D., Choukroune, P., Juteau, T., Séguret, M., Ballard, R.D., Fox, P.J., Normark, W., Carranza, A., Cordoba, D., Guerrero, J., Rangin, C., Bougault, H., Cambon, P., Hekinian, R., 1979. Massive deep sea sulphide ore deposit discovered on the East Pacific Rise. Nature 277, 523–528.

Fuchs, S., Hannington, M.D., Petersen, S., 2019. Divining gold in seafloor polymetallic massive sulfide systems. Mineral. Deposita 54, 789–820.

Gallant, R.M., Von Damm, K.L., 2006. Geochemical controls on hydrothermal fluids from the Kairei and Edmond Vent Fields, 23°–25°S, Central Indian Ridge. Geochem. Geophys. Geosystems 7, Q06018.

German, C.R., Petersen, S., Hannington, M.D., 2016. Hydrothermal exploration of mid-ocean ridges: where might the largest sulfide deposits be forming? Chem. Geol. 420, 114–126.

Grant, H.L., Hannington, M.D., Petersen, S., Frische, M., Fuchs, S.H., 2018. Constraints on the behavior of trace elements in the actively-forming TAG deposit, Mid-Atlantic Ridge, based on LA-ICP-MS analyses of pyrite. Chem. Geol. 498, 45–71.

Halbach, P., Auzende, J.M., Tuerkay, M., Allspach, A., Becker, K., et al., 1996. The Indian Ocean, future area for drilling activities. Poster-Eurocolloquium-ODP Meeting 47–48.

Halbach, P., Blum, N., Münch, U., Plüger, W., Garbe-Schönberg, D., Zimmer, M., 1998. Formation and decay of a modern massive sulfide deposit in the Indian Ocean. Mineral. Deposita 33, 302–309.

Hannington, M.D., 1989. The geochemistry of gold in modern seafloor hydrothermal systems and implication for gold mineralization in ancient volcanogenic massive sulfides (Unpublished PhD thesis). University of Toronto Canada, 544.

Hannington, M.D., 2014. Volcanogenic massive sulfide deposits. In: Scott, S.D. (Ed.), Treatise on Geochemistry, Vol. 13: Geochemistry of Mineral Deposits, 2nd ed. Elsevier, Amsterdam, pp. 463–488.

Hannington, M., Herzig, P., Scott, S., Thompson, G., Rona, P., 1991a. Comparative mineralogy and geochemistry of gold-bearing sulfide deposits on the mid-ocean ridges. Mar. Geol. 101, 217–248.

Hannington, M.D., Herzig, P.M., Scott, S.D., 1991b. Auriferous hydrothermal precipitates on the modern seafloor. In: Foster, R.P. (Ed.), Gold Metallogeny and Exploration. Blackie and Son, Glasgow, pp. 249–282.

Hannington, M.D., Tivey, M.K., Larocque, A.C., Petersen, S., Rona, P., 1995. The occurrence of gold in sulfide deposits of the TAG Hydrothermal Field, Mid-Atlantic Ridge. Can. Mineral. 33, 1285–1310.

Hannington, M.D., Petersen, S., Herzig, P.M., Jonasson, I.R., 2004. A Global Database of Seafloor Hydrothermal Systems, Including a Digital Database of Geochemical Analyses of Seafloor Polymetallic Sulfides. Geological Survey of Canada, Open File 4598, 1 CD-ROM.

Hannington, M.D., de Ronde, C.E.J., Petersen, S., 2005. Sea-floor tectonics and submarine hydrothermal systems. Econ. Geol. 111–141 100th Anniversary Volume.

Hannington, M.D., Jamieson, J., Monecke, T., Petersen, S., Beaulieu, S., 2011. The abundance of seafloor massive sulfide deposits. Geology 39, 1155–1158.

Holwell, D.A., Adeyemi, Z., Ward, L.A., Smith, D.J., Graham, S.D., McDonald, I., Smith, J.W., 2017. Low temperature alteration of magmatic Ni-Cu-PGE sulfides as a source for hydrothermal Ni and PGE ores: a quantitative approach using automated mineralogy. Ore Geol. Rev. 91, 718–740.

Huston, D.L., Sie, S.H., Suter, G.F., Cooke, D.R., Both, R.A., 1995. Trace elements in sulfide minerals from eastern Australian volcanic-hosted massive sulfide deposits: Part I. Proton microprobe analyses of pyrite, chalcopyrite, and sphalerite, and Part II. Selenium levels in pyrite: comparison with $\delta^{34}S$ values and implications for the source of sulfur in volcanogenic hydrothermal systems. Econ. Geol. 90, 1167–1196.

Janecky, D.R., Seyfried Jr., W.E., 1984. Formation of massive sulfide deposits on oceanic ridge crests: Incremental reaction models for mixing between hydrothermal solutions and seawater. Geochim. Cosmochim. Acta 48, 2723–2738.

Janecky, D.R., Seyfried Jr., W.E., 1986. Hydrothermal serpentinization of peridotite within the oceanic crust: Experimental investigations of mineralogy and major element chemistry. Geochim. Cosmochim. Acta 50, 1357–1378.

Jean-Baptiste, P., Charlou, J.L., Stievenard, M., Donval, J.P., Bougault, H., Mevel, C., 1991. Helium and methane measurements in hydrothermal fluids from the Mid-Atlantic Ridge: the Snake pit site at 23° N. Earth Planet. Sci. Lett. 106, 17–28.

Karpov, I.K., Chudnenko, K.V., Kulik, D.A., 1997. Modeling chemical mass transfer in geochemical processes: Thermodynamic relations, conditions of equilibrium, and numerical algorithms. Am. J. Sci. 297, 767–806.

Kawasumi, S., Chiba, H., 2017. Redox state of seafloor hydrothermal fluids and its effect on sulfide mineralization. Chem. Geol. 451, 25–37.

Keith, M., Häckel, F., Haase, K.M., Schwarz-Schampera, U., Klemd, R., 2016. Trace element systematics of pyrite from submarine hydrothermal vents. Ore Geol. Rev. 72, 728–745.

Klein, F., Bach, W., 2009. Fe–Ni–Co–O–S phase relations in peridotite–seawater interactions. J. Petrol. 50, 37–59.

Klein, F., Bach, W., McCollom, T.M., 2013. Compositional controls on hydrogen generation during serpentinization of ultramafic rocks. Lithos 178, 55–69.

Knight, R.D., Roberts, S., Webber, A.P., 2018. The influence of spreading rate, basement composition, fluid chemistry and chimney morphology on the formation of gold-rich SMS deposits at slow and ultraslow mid-ocean ridges. Mineral. Deposita 53, 143–152.

Koski, R.A., Shanks, W.C., Bohrson, W.A., Oscarson, R.L., 1988. The composition of massive sulfide deposits from the sediment-covered floor of Escanaba Trough, Gorda Ridge; implications for depositional processes. Can. Mineral. 26, 655–673.
Koski, R.A., Benninger, L.M., Zierenberg, R.A., Jonasson, I.R., 1994. Composition and growth history of hydrothermal deposits in Escanaba Trough, southern Gorda Ridge. In: Morton, J.L., Zierenberg, R.A., Riess, C.A. (Eds.), Geologic, Hydrothermal, and Biologic Studies at Escanaba Trough, Gorda Ridge, Offshore Northern California. U.S. Geological Survey Bulletin 2022, pp. 293–324.
Krasnov, S.G., Poroshina, I.M., Cherkashev, G.A., 1995. Geological setting of high-temperature hydrothermal activity and massive sulphide formation on fast- and slow-spreading ridges. In: Parson, L.M., Walker, C.L., Dixon, D.R. (Eds.), Hydrothermal Vents and Processes. Geol. Soc. Lond., Spec. Publ 87, pp. 17–23.
Kumagai, H., Nakamura, K., Toki, T., Morishita, T., Okino, K., Ishibashi, J.I., Tsunogai, U., Kawagucci, S., Gamo, T., Shibuya, T., Sawaguchi, T., Neo, N., Joshima, M., Sato, T., Takai, K., 2008. Geological background of the Kairei and Edmond hydrothermal fields along the Central Indian Ridge: implications of their vent fluids' distinct chemistry. Geofluids 8, 239–251.
Lehnert, K., Su, Y., Langmuir, C., Sarbas, B., Nohl, U., 2000. A global geochemical database structure for rocks. Geochem. Geophys. Geosystems 1, 1–14.
Liao, S., Tao, C., Li, H., Barriga, F.J.A.S., Liang, J., Yang, W., Yu, J., Zhu, C., 2018. Bulk geochemistry, sulfur isotope characteristics of the Yuhuang-1 hydrothermal field on the ultraslow-spreading Southwest Indian Ridge. Ore Geol. Rev. 96, 13–27.
Liu, W., Migdisov, A., Williams-Jones, A., 2012. The stability of aqueous nickel (II) chloride complexes in hydrothermal solutions: results of UV–Visible spectroscopic experiments. Geochim. Cosmochim. Acta 94, 276–290.
Lowell, R., 2010. Hydrothermal circulation at slow spreading ridges: Analysis of heat sources and heat transfer processes. In: Rona, P.A., Devey, C.W., Dyment, J., Murton, B.J. (Eds.), Diversity of Hydrothermal Systems on Slow Spreading Ocean Ridges. Geophysical Monograph 188. American Geophysical Union, Washington DC, pp. 11–26.
Lowell, R.P., Rona, P.A., Von Herzen, R.P., 1995. Seafloor hydrothermal systems. J. Geophys. Res. Solid Earth 100, 327–352.
MacLeod, C.J., Searle, R.C., Murton, B.J., Casey, J.F., Mallows, C., Unsworth, S.C., Achenbach, K.L., Harris, M., 2009. Life cycle of oceanic core complexes. Earth Planet. Sci. Lett. 287, 333–344.
Marchig, V., Blum, N., Roonwal, G., 1997. Massive sulfide chimneys from the east pacific rise at 7 24's and 16 43's. Mar. Georesour. Geotechnol. 15, 49–66.
Marques, A.F.A., Barriga, F.J.A.S., Chavagnac, V., Fouquet, Y., 2006. Mineralogy, geochemistry, and Nd isotope composition of the Rainbow hydrothermal field, Mid-Atlantic Ridge. Mineral. Deposita 41, 52–67.
Marques, A.F.A., Barriga, F.J.A.S., Scott, S.D., 2007. Sulfide mineralization in an ultramafic-rock hosted seafloor hydrothermal system: from serpentinization to the formation of Cu–Zn–(Co)-rich massive sulfides. Mar. Geol. 245, 20–39.
Martín-Fernández, J.A., Barceló-Vidal, C., Pawlowsky-Glahn, V., 2003. Dealing with zeros and missing values in compositional data sets using nonparametric imputation. Math. Geol. 35, 253–278.
Maslennikov, V.V., Maslennikova, S.P., Large, R.R., Danyushevsky, L., 2009. Study of trace element zonation in vent chimneys from the Silurian Yaman-Kasy volcanic-hosted massive sulfide deposit (Southern Urals, Russia) using laser ablation-inductively coupled plasma mass spectrometry (LA-ICPMS). Econ. Geol. 104, 111–141.
Maslennikov, V.V., Maslennikova, S.P., Large, R.R., Danyushevsky, L.V., Herrington, R.J., Ayupova, N.R., Zaykov, V.V., Lein, A.Yu., Tseluyko, A.S., Melekestseva, I.Yu., Tessalina, S.G., 2017. Chimneys in Paleozoic massive sulfide mounds of the Urals VMS deposits: Mineral and trace element comparison with modern black, grey, white and clear smokers. Ore Geol. Rev. 85, 64–106.
McCollom, T.M., Shock, E.L., 1998. Fluid-rock interactions in the lower oceanic crust: Thermodynamic models of hydrothermal alteration. J. Geophys. Res. Solid Earth 103 (B1), 547–575.
McDermott, J.M., Sylva, S.P., Ono, S., German, C.R., Seewald, J.S., 2018. Geochemistry of fluids from Earth's deepest ridge-crest hot-springs: Piccard hydrothermal field, Mid-Cayman Rise. Geochim. Cosmochim. Acta 228, 95–118.
Melekestseva, I.Yu., Zaykov, V.V., Nimis, P., Tret'yakov, G.A., Tesalina, S.G., 2013. Cu-(Ni-Co-Au)–bearing massive sulfide deposits associated with mafic-ultramafic rocks of the Main Urals fault, South Urals: Geological structures, ore textural and mineralogical features, comparison with modern analogs. Ore Geol. Rev. 52, 18–36.
Melekestseva, I.Yu., Tret'yakov, G.A., Nimis, P., Yuminov, A.M., Maslennikov, V.V., Maslennikova, S.P., Kotlyarov, V.A., Beltenev, V.E., Danyushevsky, L.V., Large, R., 2014. Barite-rich massive sulfides from the Semenov-1 hydrothermal field (Mid-Atlantic Ridge, 13°30.87'N): evidence for phase separation and magmatic input. Mar. Geol. 349, 37–54.
Melekestseva, I.Yu., Maslennikov, V.V., Tret'yakov, G.A., Nimis, P., Beltenev, V.E., Rozhdestvenskaya, I.I., Maslennikova, S.P., Belogub, E.V., Danyushevsky, L., Large, R., Yuminov, A.M., Sadykov, S.A., 2017. Gold-and Silver-Rich Massive Sulfides from the Semenov-2 Hydrothermal Field, 13° 31.13'N, Mid-Atlantic Ridge: a Case of Magmatic Contribution? Econ. Geol. 112, 741–773.
Moss, R., Scott, S.D., 1996. Silver in sulfide chimneys and mounds from 13° N and 21° N, East Pacific Rise. Can. Mineral. 34, 697–716.
Mottl, M.J., 2003. Partitioning of energy and mass fluxes between mid-ocean ridges axes and flanks at high and low temperature. In: Halbach, P.E., Tunnicliffe, V., Hein, J.R. (Eds.), Energy and Mass Transfer in Marine Hydrothermal Systems. Dahlem University Press, Berlin, pp. 271–286.
Murphy, P.J., Meyer, G., 1998. A gold-copper association in ultramafic-hosted hydrothermal sulfides from the Mid-Atlantic Ridge. Econ. Geol. 93, 1076–1083.
Nagaseki, H., Hayashi, K.I., 2008. Experimental study of the behavior of copper and zinc in a boiling hydrothermal system. Geology 36, 27–30.
Palandri, J.L., Reed, M.H., 2004. Geochemical models of metasomatism in ultramafic systems: Serpentinization, rodingitization, and sea floor carbonate chimney precipitation. Geochim. Cosmochim. Acta 68, 1115–1133.
Palarea-Albaladejo, J., Martín-Fernández, J.A., 2015. zCompositions—R package for multivariate imputation of left-censored data under a compositional approach. Chemom. Intell. Lab. Syst. 143, 85–96.
Patten, C.G., Pitcairn, I.K., Teagle, D.A., Harris, M., 2016. Sulphide mineral evolution and metal mobility during alteration of the oceanic crust: Insights from ODP Hole 1256D. Geochim. Cosmochim. Acta 193, 132–159.
Pester, N.J., Rough, M., Ding, K., Seyfried, W.E., 2011. A new Fe/Mn geothermometer for hydrothermal systems: implications for high-salinity fluids at 13°N on the East Pacific Rise. Geochim. Cosmochim. Acta 75, 7881–7892.
Petersen, S., 2000. The Geochemical and Mineralogical Evolution of the TAG Hydrothermal Field, Mid-Atlantic Ridge, 26° N (Unpublished PhD thesis). TU Bergakademie Freiberg Freiberg, Germany.
Petersen, S., Hein, J.R., 2013. The geology of sea-floor massive sulphides. In: In: Baker, E., Beaudoin, Y. (Eds.), Deep Sea Minerals: Sea-Floor Massive Sulphides, a Physical, Biological, Environmental, and Technical Review, vol. 1A Secretariat of the Pacific Community.
Pokrovski, G.S., Roux, J., Harrichoury, J.C., 2005. Fluid density control on vapor-liquid partitioning of metals in hydrothermal systems. Geology 33, 657–660.
Pokrovski, G.S., Borisova, A.Y., Harrichoury, J.C., 2008. The effect of sulfur on vapor–liquid fractionation of metals in hydrothermal systems. Earth Planet. Sci. Lett. 266, 345–362.
Reimann, C., Filzmoser, P., Garrett, R.G., 2002. Factor analysis applied to regional geochemical data: problems and possibilities. Appl. Geochem. 17, 185–206.
Reimann, C., Filzmoser, P., Garrett, R.G., Dutter, R., 2008. Statistical Data Analysis Explained: Applied Environmental Statistics with R. John Wiley & Sons, Chichester, UK, pp. 343.
Rona, P.A., Bogdanov, Y.A., Gurvich, E.G., Rimski-Korsakov, N.A., Sagalevitch, A.M., Hannington, M.D., Thompson, G., 1993. Relict hydrothermal zones in the TAG hydrothermal field, Mid-Atlantic Ridge 26° N, 45° W. J. Geophys. Res. Solid Earth 98, 9715–9730.
Safina, N.P., Melekestseva, I.Yu., Nimis, P., Ankusheva, N.N., Yuminov, A.M., Kotlyarov, V.A., Sadykov, S.A., 2016. Barite from the Saf'yanovka VMS deposit (Central Urals) and Semenov-1 and -3 hydrothermal sulfide fields (Mid-Atlantic Ridge): a comparative analysis of formation conditions. Mineral. Deposita 51, 491–507.
Samson, J., 1986. Compilation of Information on Polymetallic Sulfide Deposits and Occurrences off the West Coast of Canada. Canada Oil and Gas Lands Administration, pp. 1–58.
Seewald, J.S., Seyfried, W.E., 1990. The effect of temperature on metal mobility in subseafloor hydrothermal systems: constraints from basalt alteration experiments. Earth Planet. Sci. Lett. 101, 388–403.
Seewald, J.S., Cruse, A.M., Saccocia, P.J., 2003. Aqueous volatiles in hydrothermal fluids from the Main Endeavour Field, northern Juan de Fuca Ridge: temporal variability following earthquake activity. Earth Planet. Sci. Lett. 216, 575–590.
Seyfried, W.E., Dibble, W.E., 1980. Seawater-peridotite interaction at 300 °C and 500 bars: implications for the origin of oceanic serpentinites. Geochim. Cosmochim. Acta 44, 309–321.
Seyfried, W., Bischoff, J.L., 1977. Hydrothermal transport of heavy metals by seawater: the role of seawater/basalt ratio. Earth Planet. Sci. Lett. 34, 71–77.
Seyfried, W.E., Ding, K., 1995. Phase equilibria in subseafloor hydrothermal systems: A review of the role of redox, temperature, pH and dissolved Cl on the chemistry of hot spring fluids at mid-ocean ridges. In: In: Humphris, S.E., Zierenberg, R.A., Mullineaux, L.S., Thomson, R.E. (Eds.), Seafloor Hydrothermal Systems: Physical, Chemical, Biological, and Geological Interactions, AGU Geophysical Monograph, vol. 91. pp. 248–272.
Seyfried Jr., W.E., Shanks, W.C., 2004. Alteration and mass transport in mid-ocean ridge hydrothermal systems: Controls on the chemical and isotopic evolution of high-temperature crustal fluids. In: Davis, E., Elderfield, H. (Eds.), Hydrogeology of the Oceanic Lithosphere. Cambridge University Press, Cambridge, pp. 451–495.
Seyfried Jr., W.E., Bischoff, J.L., 1981. Experimental seawater-basalt interaction at 300° C, 500 bars, chemical exchange, secondary mineral formation and implications for the transport of heavy metals. Geochim. Cosmochim. Acta 45, 135–147.
Seyfried Jr., W.E., Janecky, D.R., 1985. Heavy metal and sulfur transport during subcritical and supercritical hydrothermal alteration of basalt: Influence of fluid pressure and basalt composition and crystallinity. Geochim. Cosmochim. Acta 49, 2545–2560.
Seyfried Jr., W.E., Mottl, M.J., 1982. Hydrothermal alteration of basalt by seawater under seawater-dominated conditions. Geochim. Cosmochim. Acta 46, 985–1002.
Seyfried, W.E., Berndt, M.E., Seewald, J.S., 1988. Hydrothermal alteration processes at mid-ocean ridges; constraints from diabase alteration experiments, hot spring fluids and composition of the oceanic crust. Can. Mineral. 26, 787–804.
Seyfried, W.E., Pester, N.J., Ding, K., Rough, M., 2011. Vent fluid chemistry of the Rainbow hydrothermal system (36 N, MAR): phase equilibria and in situ pH controls on subseafloor alteration processes. Geochim. Cosmochim. Acta 75, 1574–1593.
Sharp, T.G., Buseck, P.R., 1993. The distribution of Ag and Sb in galena: Inclusions versus solid solution. Am. Mineral. 78, 85–95.
Sleep, N.H., 1983. Hydrothermal convection at ridge axes. In: Rona, P.A., Boström, K., Laubier, L., Smith, K.L.Jr (Eds.), Hydrothermal Processes of Seafloor Spreading Centers. Springer-Verlag, New York, pp. 71–82.
Steele, J.H., Thorpe, S.A., Turekian, K.K., 2010. Encyclopedia of Ocean Sciences, Second Edition: Appendix 3, Estimated Mean Oceanic Concentration of the Elements. Elsevier, Amsterdam, pp. 602–603.
Templ, M., Hron, K., Filzmoser, P., 2011. robCompositions: an R-package for robust statistical analysis of compositional data. In: Pawlowsky-Glahn, V., Buccianti, A. (Eds.), Compositional Data Analysis. Theory and Applications. John Wiley & Sons, Chichester, UK, pp. 341–355.

Tivey, M.K., 1995. The influence of hydrothermal fluid composition and advection rates on black smoker chimney mineralogy: insights from modeling transport and reaction. Geochim. Cosmochim. Acta 59, 1933–1949.
Tivey, M.K., 2007. Generation of seafloor hydrothermal vent fluids and associated mineral deposits. Oceanography 20, 50–65.
Tivey, M.K., Humphris, S.E., Thompson, G., Hannington, M.D., Rona, P.A., 1995. Deducing patterns of fluid flow and mixing within the TAG active hydrothermal mound using mineralogical and geochemical data. J. Geophys. Res. Solid Earth 100 (B7), 12527–12555.
Tivey, M.K., Stakes, D.S., Cook, T.L., Hannington, M.D., Petersen, S., 1999. A model for growth of steep-sided vent structures on the Endeavour Segment of the Juan de Fuca Ridge: results of a petrologic and geochemical study. J. Geophys. Res. Solid Earth 104, 22859–22883.
Vaughan, D.J., Rosso, K.M., 2006. Chemical bonding in sulfide minerals. In: In: Vaughan, D.J. (Ed.), Sulfide Mineralogy and Geochemistry, Rev. Mineral. Geochem, vol. 61. pp. 231–264.
Wang, Y., Han, X., Petersen, S., Jin, X., Qiu, Z., Zhu, J., 2014. Mineralogy and geochemistry of hydrothermal precipitates from Kairei hydrothermal field, Central Indian Ridge. Mar. Geol. 354, 69–80.
Wang, Y., Han, X., Petersen, S., Frische, M., Qiu, Z., Cai, Y., Zhou, P., 2018. Trace metal distribution in sulfide minerals from ultramafic-hosted hydrothermal systems: examples from the Kairei Vent Field, Central Indian Ridge. Minerals 8, 526.
Webber, A.P., Roberts, S., Murton, B.J., Hodgkinson, M.R., 2015. Geology, sulfide geochemistry and supercritical venting at the Beebe Hydrothermal Vent Field, Cayman Trough. Geochem. Geophys. Geosystems 16, 2661–2678.
Wedepohl, K.H., 1969. Handbook of Geochemistry, vol. II Springer-Verlag, Berlin.
Wetzel, L.R., Shock, E.L., 2000. Distinguishing ultramafic-from basalt-hosted submarine hydrothermal systems by comparing calculated vent fluid compositions. J. Geophys. Res. Solid Earth 105 (B4), 8319–8340.
Wilcock, W.S., Delaney, J.R., 1996. Mid-ocean ridge sulfide deposits: evidence for heat extraction from magma chambers or cracking fronts? Earth Planet. Sci. Lett. 145, 49–64.
Wohlgemuth-Ueberwasser, C.C., Viljoen, F., Petersen, S., Vorster, C., 2015. Distribution and solubility limits of trace elements in hydrothermal black smoker sulfides: an in-situ LA-ICP-MS study. Geochim. Cosmochim. Acta 159, 16–41.
Wu, Z., Sun, X., Xu, H., Konishi, H., Wang, Y., Wang, C., Dai, Y., Deng, X., Yu, M., 2016. Occurrences and distribution of “invisible” precious metals in sulfide deposits from the Edmond hydrothermal field, Central Indian Ridge. Ore Geol. Rev. 79, 105–132.
Zaccarini, F., Garuti, G., 2008. Mineralogy and chemical composition of VMS deposits of northern Apennine ophiolites, Italy: evidence for the influence of country rock type on ore composition. Mineral. Petrol. 94, 61–83.
Zierenberg, R.A., Shanks III, W.C., Bischoff, J.L., 1984. Massive sulfide deposits at 21° N, East Pacific rise: Chemical composition, stable isotopes, and phase equilibria. Geol. Soc. Am. Bull. 95, 922–929.